MOX-Report No. 26/2018

Extended Finite Elements method for fluid-structure interaction with an immersed thick non-linear structure

Vergara, C.; Zonca, S.

MOX, Dipartimento di Matematica
Politecnico di Milano, Via Bonardi 9 - 20133 Milano (Italy)

mox-dmat@polimi.it http://mox.polimi.it

Extended Finite Elements method for fluid-structure interaction with an immersed thick non-linear structure

C. Vergara[♯], S. Zonca[♯]

April 15, 2018

[♯] MOX– Modellistica e Calcolo Scientifico
Dipartimento di Matematica
Politecnico di Milano
via Bonardi 9, 20133 Milano, Italy
<christian.vergara,stefano.zonca>@mate.polimi.it

Keywords: Fluid-structure interaction, unfitted meshes, valve dynamics

AMS Subject Classification: 65M60 , 74F10

Abstract

We consider an Extended Finite Element method to solve fluid-structure interaction problems in the case of an immersed thick structure described by non-linear finite elasticity. This method, that belongs to the family of the Cut Finite Element methods, allows to consider unfitted meshes for the fluid and solid domains by maintaining the fluid mesh fixed in time as the solid moves. We review the state of the art about the numerical methods for fluid-structure interaction problems and we present an overview of the Cut Finite Element methods. We describe the numerical discretization proposed here to handle the case of a thick immersed structure with size comparable or smaller than the fluid mesh element size in the case of non-linear finite elasticity. Finally, we present some three-dimensional numerical results of the proposed method.

1 Introduction

The interaction between a fluid and an immersed structure may be significant in many applications, for example in aeronautic engineering to study the response of the air on the aircraft [11, 32, 33, 61], in civil engineering to understand the effect of wind on bridges [20, 74, 92], towers [54], and suspended cable [13, 81], in energy engineering to study the modeling of wind-turbines, heat exchangers and hydro-turbines [9, 80, 85], in sport engineering to investigate the impact of the waves over a rowing boat [34, 35] or the flow around a sailing yatch [78], in biomedical application, for instance in

hemodynamics to study the stresses exerted by blood flow to the leaflets of an heart valve [67, 89], or to study the blood pressure exerted to the retinal vessels walls [3, 5].

In some cases, it may be interesting to consider a *full three-dimensional* (3D) model for the structure, even though the thickness of the structure is small with respect to the characteristic size of the domain. For example, in the simulation of heart valves, one should consider the interaction between the blood and the valve leaflets. Often, for clinical purposes, there is the need to accurately evaluate the internal structural stresses, which can be computed only by means of a full 3D geometric model.

The numerical simulation of such a fluid-structure interaction problem is very challenging. First of all, the structure undergoes large displacements, thus its movement cannot be ignored from the geometric point of view. Second, the immersed structure is very thin, often smaller than the characteristic mesh size of the fluid problem, and this leads to numerical and computational difficulties due to the cut of some fluid mesh elements.

In this work, we propose an *Extended Finite Elements* discretization for FSI problem with an immersed 3D non-linear elastic structure in the regime of large displacements. In Sect. 2 we briefly review the most important numerical strategies introduced so far to handle this problem, whereas in Sect. 3 we specifically focus on the family of *Cut Finite Elements*, to which our method belongs. Then, in Sect. 4 we introduce the mathematical problem and the proposed numerical approximation, whereas in Sect. 5 we give some detail on the algorithm for the solution of the non-linear system arising after discretization. Finally, in Sect. 6 we present some numerical results.

2 State of the art

Several numerical methods have been developed so far to solve the FSI problem with an immersed structure. We subdivide them depending on the treatment of the computational meshes. Accordingly, we arrange them into two main categories: *body-fitted* mesh methods and *fixed/unfitted* mesh methods.

In the first category, we place all the methods that use a conforming and fitted mesh at the fluid-structure interface. Among them, we cite the *Arbitrary Lagrangian Eulerian* approach introduced in [29,55,58]. In presence of very large displacements, this method may fail due to the high distortion of the fluid mesh, so that a remeshing procedure is required. Moreover, this procedure has the disadvantage that may introduce an artificial diffusivity due to the need of interpolating from one mesh to the new one. Nonetheless, the ALE method has been used by some authors to deal with immersed structures. For example, in [64] an ALE approach with remeshing is proposed to simulate heart valve closure on a 2D simplified geometry, in [75] a synthetic 3D model was employed to study the valve opening, in [63] a 3D model is used to study the influence of the sinus of Valsalva in the aortic valve, in [91] a 2D simulation of the aortic valve is performed on a plane of symmetry along the center of a leaflet for an entire cardiac cycle. A similar approach based on local adaptation is presented in [8]. This "Extended ALE" method allows the structure mesh to move independently of the fluid one that is kept fixed,

resulting in a pair of meshes that are not fitted at the interface. Then, the fitting between the two meshes is obtained via local remeshing or local changes in the connectivity.

Another fitted method is given by *Space-Time Finite Elements* [30, 57, 59, 76]. The basic idea is to divide the time domain into slabs and then to use the Finite Element (FE) basis functions on each slab for both the spatial and temporal discretizations.

In the second family of numerical methods, we place the methods based on a fixed background mesh and on an overlapped unfitted mesh for the fluid and the solid, respectively. These approaches were developed to avoid the movement, or the remeshing, of the fluid mesh. In particular, they have been specifically designed for treating the case of large deformations.

The first fixed/unfitted mesh method proposed in the literature is the *Immersed Boundary* (IB) method, introduced in [79] in the context of Finite Differences for an immersed membrane and specifically realized for studying the fluid-dynamics in the heart. In this framework, the fluid is represented in Eulerian coordinates, while the structure in Lagrangian coordinates by means of a forcing term for the fluid problem that acts on the fluid-structure interface. The extension of the IB approach to the FE method is presented in [15, 16]. The FE formulation is extendable to the case of thick structures and allows to easily manage the forcing term given by the action of the structure on the fluid, see, e.g., [17, 90, 94]. As regards the applications, the Finite Difference IB method has been used in [47] to simulate the blood dynamics in a realistic domain of the heart and in [46, 48] to simulate the dynamics of the heart valves. The Finite Element IB method has been employed in [93] to study an immersed structure interacting with a viscous fluid and in [66] for several biological applications regarding valve dynamics, vessel stents, red blood cells interaction and cells migrations. See also [56] for an application to bioprosthetic heart valves. Another IB approach widely used in the context of heart valves is the *Curvilinear Immersed Boundary* (CURVIB) method [36] which is particularly suited for the 3D case. The CURVIB method was successfully employed for FSI problems for simulating the dynamics of prosthetic heart valves, see [18, 19, 36, 65].

A different approach in the category of the fixed/unfitted mesh methods is the *Fictitious Domain* (FD) method. This method was introduced in [43] for solving the viscous-plastic flow equations inside complex domains, then in [14, 44] it was used for solving the Navier-Stokes equations around immersed objects, and in [45] it was extended to treat the case of moving rigid bodies inside incompressible viscous flows with applications to particle flows, see also [41, 42]. Several works based on the FD method have been produced for the solution of FSI problems with immersed structures: in [86, 87] an application to FSI for heart valves including contact with rigid bodies is presented; in [7] a procedure for dealing with the interaction of an incompressible fluid and different structures is proposed, allowing the contact among the deformable bodies; in [83] an application for heart valves is compared with experimental data; in [62] an application to bioprosthetic heart valves is considered; in [88] a comparison of some FD approaches with the ALE one is presented for several FSI problems. A variant to the FD approach for dealing with valve dynamics is proposed in [26, 27]. In the latter works, the FD approach is combined with the ALE one in order to exploit their advantages: the ALE approach is used to describe the movement of the root of the valve, that

undergoes a limited displacement, so that no remeshing is necessary, allowing to build a fitted mesh at the fluid-structure interface; the FD approach is instead used to describe the leaflets of the valve that, on the contrary, undergo large displacements.

3 Cut Finite Element methods

The methods presented above feature two main limitations:

- the body-fitted mesh methods require the remeshing of the fluid domain due to the highly distorted fluid elements that appear when the displacement of the immersed structure is too large;
- the fixed/unfitted mesh methods require the implementation of ad-hoc strategies to sharply capture the interface. Indeed, in the case of "diffuse interface" methods (such as the IB method), the interface conditions are imposed through forcing terms which spread the effect of such conditions on a cluster of neighbouring cells. This results in a lack of sharpness in capturing the boundaries and the inability of enforcing boundary conditions for strongly fluctuating quantities, such as in turbulent flows, see, e.g., [72].

Here, we consider a specific class of methods belonging to the fixed/unfitted family that tries to overcome these limitations. The advantages of this class, referred to as *Cut Finite Element* (CFE) methods, are that they maintain the accuracy of classical FEM and can be developed by extending the features of FEM, see, e.g., [22] for a review of this class of methods.

Let us consider a finite set of domains $\Omega^i \in \mathbb{R}^d$, with $i = 1,\dots,N$, and $d = 3$. We indicate with

- *background* domain, a domain Ω such that $\Omega \supseteq \bigcup_{i=1}^{N} \Omega^i$, i.e. a domain that covers all the domains Ω^i;
- *foreground* domain, each of the domains Ω^i, $i = 1,\dots,N$, that overlaps the background domain Ω;
- *interface*, a curve Σ^i, $i = 1,\dots,N$, of co-dimension one that separates the background domain Ω to the foreground domain Ω^i.

Moreover, we distinguish the foreground domains into three categories, depending on their thickness:

- *zero-thickness* domain, a foreground domain of co-dimension one (contained in the background domain Ω) that divides Ω into two parts (Σ in Figure 1);
- *thin* domain, a foreground domain such that its thickness is smaller than the characteristic size of the background mesh (Ω^1 in Figure 1);
- *thick* domain, a foreground domain Ω^i such that the thickness of the domain is comparable with its characteristic size (Ω^2 in Figure 1).

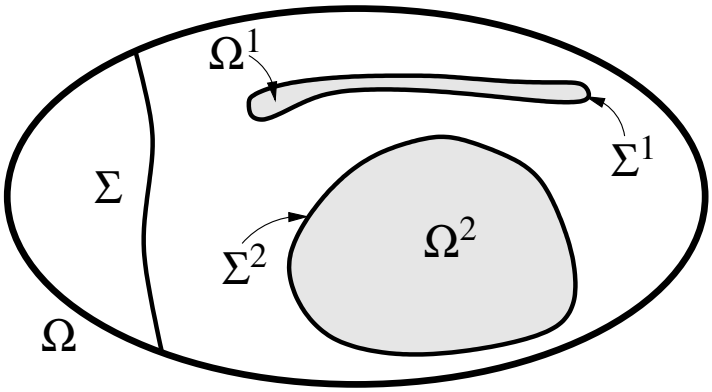

Figure 1: The background domain Ω (white) contains the zero-thickness domain Σ, the thin foreground domain Ω^1 (grey) and the thick foreground domain Ω^2 (grey). The interfaces Σ^1 and Σ^2 delimit Ω^1 and Ω^2, respectively.

With the final aim of describing how the physical processes are related to the domains and the meshes, in what follows we consider two processes, P^B and P^F, that represent the *background* and *foreground processes*, respectively. Process P^B occurs in the *background process domain* Ω^{BP}, while process P^F occurs in the *foreground domain* Ω^F, see Figure 2 (top). The union of the domains Ω^{BP} and Ω^F generates the *background domain* Ω, see Figure 2 (bottom).

For each of these three domains we generate the corresponding mesh. In particular, for the background domain Ω, we generate the *background mesh* $\mathscr{T}_h$, and for the foreground domain Ω^F, we generate the *foreground mesh* $\mathscr{T}_h^F$, see Figure 3 (top). The *background process mesh* $\mathscr{T}_h^{BP}$ is instead generated by considering only the portions of the elements of the background mesh $\mathscr{T}_h$ that belong to the background process domain Ω^{BP}, see Figure 3 (bottom), i.e.

$$\mathscr{T}_h^{BP} = \{K : K = K'_{|\Omega^{BP}}, \forall K' \in \mathscr{T}_h\}. \tag{1}$$

We have indicated by $h > 0$ the mesh size. Notice that the background process mesh contains elements of arbitrary shape, in particular polygons. We also define by $\widetilde{\mathscr{T}}_h^{BP}$ the smallest mesh contained in $\mathscr{T}_h$ that covers the background process domain Ω^{BP} as

$$\widetilde{\mathscr{T}}_h^{BP} = \{K \in \mathscr{T}_h : K \cap \Omega^{BP} \neq \emptyset\}, \tag{2}$$

i.e. $\widetilde{\mathscr{T}}_h^{BP}$ is composed by the elements K that belong (also partially) to the domain Ω^{BP}, see Figure 4 (left). Finally, we define by $\widetilde{\Omega}^{BP}$ the domain associated with the mesh $\widetilde{\mathscr{T}}_h^{BP}$, see Figure 4 (right), i.e.

$$\widetilde{\Omega}^{BP} = int\left(\bigcup_{K \in \widetilde{\mathscr{T}}_h^{BP}} K\right). \tag{3}$$

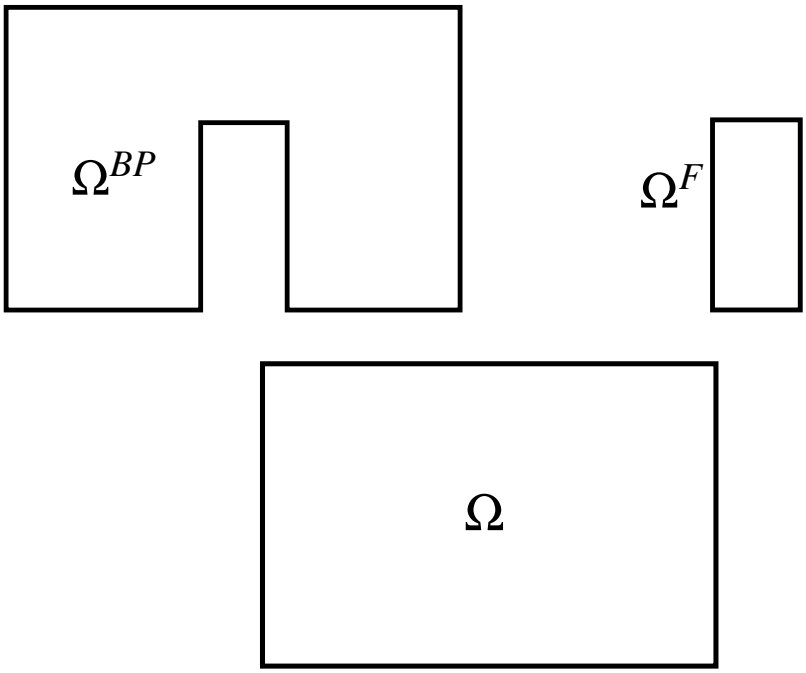

Figure 2: Top, left: the background process domain Ω^{BP} associated with the process P^B. Top, right: the foreground domain Ω^F associated with the process P^F. Bottom: the background domain Ω is the union of the background process domain Ω^{BP} and the foreground domain Ω^F.

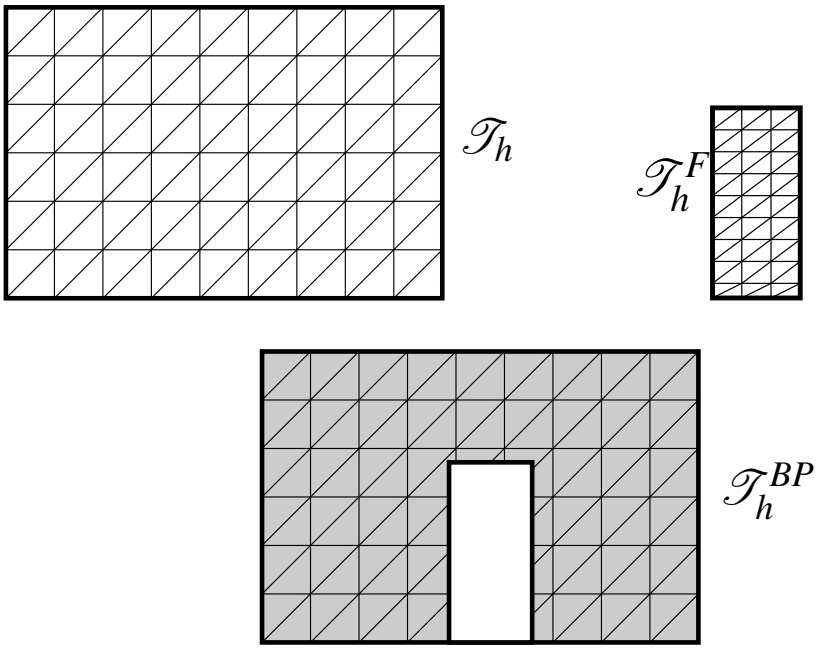

Figure 3: Top, left: the background mesh $\mathscr{T}_h$ related to the background domain Ω. Top, right: the foreground mesh $\mathscr{T}_h^F$ related to the foreground domain Ω^F. Bottom: the background process mesh $\mathscr{T}_h^{BP}$ (grey) associated with the background process domain P^B.

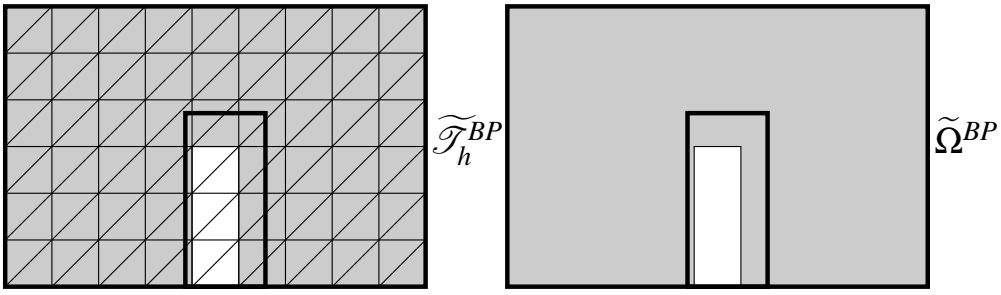

Figure 4: Left: the mesh $\widetilde{\mathscr{T}}_h^{BP}$ (grey). Right: the domain $\widetilde{\Omega}^{BP}$ (grey).

With the above definitions, we can provide the following statement:

The common idea of Cut Finite Element methods is

i) *to take a fixed background mesh overlapped by foreground meshes,*

ii) *to cut the elements of the background mesh with the zero-thickness mesh or with the interfaces of the thin and thick foreground meshes, generating elements of arbitrary shape (polytopes), and*

iii) *to write a suitable weak formulation within the background process and foreground domains.*

We stress that the nature of the foreground domain may be either *geometric* or *physical*. In particular:

- for a geometric foreground domain, the zero-thickness domain describes a discontinuity in the properties of the background domain, but it is not subject to a process; instead, the thin and thick domains may represent *i)* either a portion of the space with different physical properties with respect to the background one, however being described by the same process, *ii)* or a "hole" in the background geometry that is not subject to any process (*empty process*);

- for a physical foreground domain, the zero-thickness, thin and thick domains represent a different physical process with respect to the background one, represented by a different partial differential equation, as it happens in the FSI problem.

Different formulations have been proposed depending on the thickness and nature of the foreground domains, and each of these leads to a different CFE method. A graphical representation of all the possible combinations in the case of two processes is shown in Table 1. In the literature, the geometric cases are considered in the following works: the zero-thickness case is treated in [4, 12, 49, 73] for elliptic problems, in [10, 50, 77] for solid mechanics and in [52] for the Stokes problem; the thin case is treated in [82] for solving the Navier-Stokes equations; the thick case is considered in [51, 68] for elliptic problems and in [69] for the Stokes problem. The physical cases have been studied in the following works for FSI problems: the zero-thickness case in [2]; the thin case in [37–39] in a two-dimensional framework and in [95] for 3D problems; the thick case in [23] in two-dimensions, and in [37, 40, 70, 71] in three-dimensions. A particular physical case is considered in [53, 60] for solving PDEs only on the zero-thickness foreground domain, i.e. on immersed surfaces.

In particular, the thickness of the foreground domain has a strong effect on the approach employed to tackle the problem in the background process domain. In fact, when a foreground domain crosses the elements of the background mesh, three different configurations may appear, see Figure 5.

In the case of a zero-thickness domain Σ, see Figure 5 (left), the background element K is split into two parts and a numerical approximation is required on each portion of

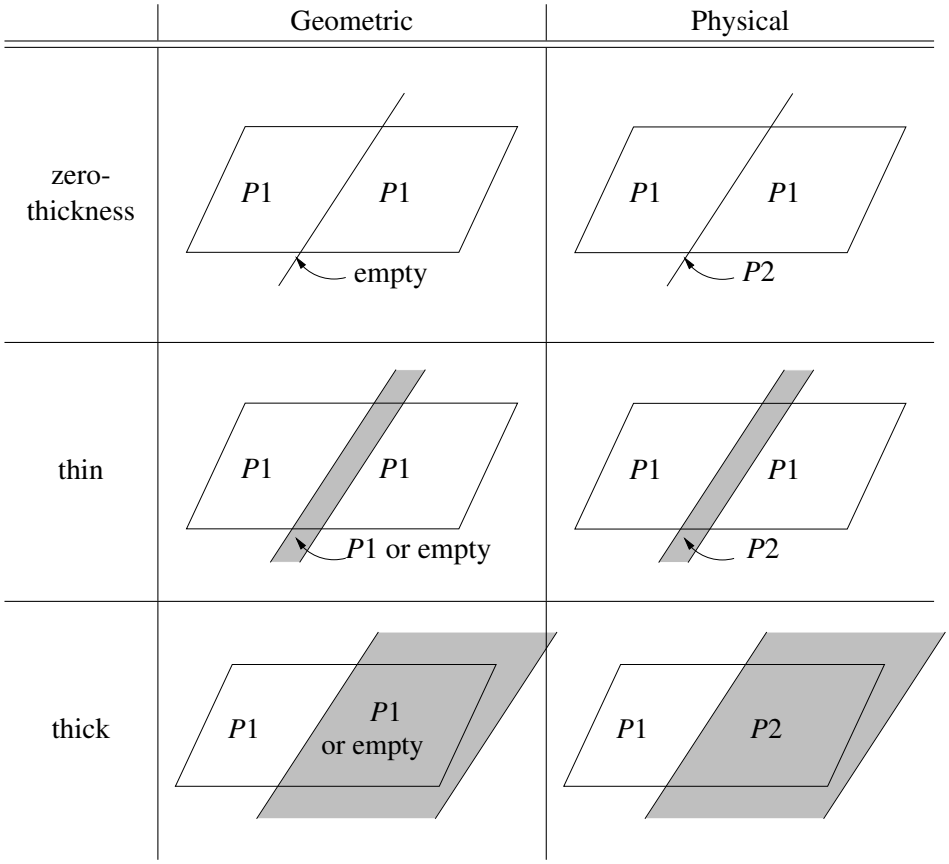

Table 1: Schematic representation of possible scenarios when considering overlapping background (white) and foreground (grey) domains. On each resulting domain, we have indicated the underlying process ($P1$, $P2$ or empty).

K. In the case of a thin domain Ω^1, see Figure 5 (center), the background element K is partially overlapped and is divided into three parts: only the two parts that belong to the background process domain require a numerical approximation for the background process. Finally, in the case of thick domain Ω^2, see Figure 5 (right), the background element K is divided into two portions and the numerical solution for the background process is required only on the background process mesh.

In any case, conforming grids at the interface between the background and foreground domains are difficult to generate, since the immersed foreground domain provides a severe constraint for the mesh generation. For this reason, unfitted overlapping meshes are considered in order to avoid the computational issue that may arise when generating fitted meshes.

The conditions to couple the problem at the interface are usually imposed via the *Discontinuous Galerkin* (DG) method (or, as some authors refer to, the *Nitsche*'s method). Lagrange multipliers are also considered, see, e.g., [37–40].

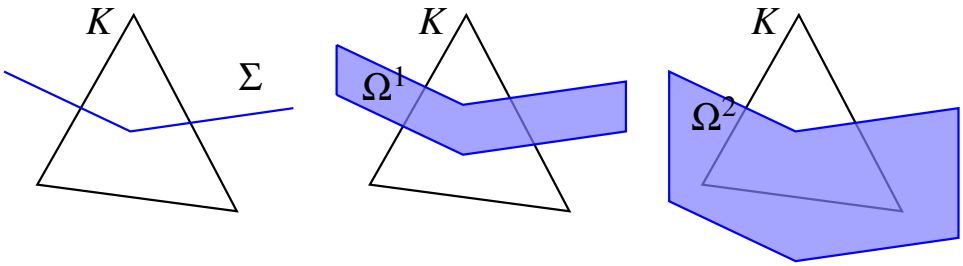

Figure 5: Configurations of the background element K depending on the thickness of the foreground domain. Left: a foreground zero-thickness domain Σ intersects the background element K. Center: a thin foreground domain Ω^1 overlaps the background element K. Right: a thick foreground domain Ω^2 overlaps the background element K. In white, the background process element.

The majority of the methods presented above allow to consider a background domain overlapped by a thick foreground domain or crossed by a zero-thickness foreground domain. However, they do not deal with the case of a thin foreground domain immersed in the background one and, in fact, the extension of these methods to the thin case is not straightforward, since the thickness of the foreground domain is smaller than the characteristic size of the background mesh elements. Some works in this direction has been proposed in the literature: in [38–40], the authors consider two and three-dimensional approaches that are able to combine the feature of the *Extended Finite Element method* (XFEM) with overlapping meshes in the case of thin and thick foreground domains, by employing Lagrange multipliers for imposing the interface conditions; in [82] a method has been proposed to solve the Navier-Stokes equation solely with immersed fixed obstacles in a three-dimensional framework, where the interface conditions are imposed via the Nitsche's method. Recently, in [95], an XFEM method to handle the case of a thin foreground domain for 3D computations has been proposed for a linear structure.

The goal of this work is to describe a method for solving three-dimensional FSI problems with a non-linear immersed thin structure that combine the features of the approaches presented above, i.e. *i)* the possibility of considering a numerical solution in each portion of the fluid background elements split by the interface and *ii)* the employment of composite grids to represent two domains, see Figure 6.

4 The continuous problem and the Extended Finite Elements approximation

We consider a fluid background process domain $\Omega^{BP} = \Omega^f$ and a structure foreground domain $\Omega^F = \Omega^s$ such that $\Omega = \Omega^f \cup \Omega^s \subset \mathbb{R}^d$, $d = 2,3$, is the background domain and $\Sigma = \overline{\Omega}^f \cap \overline{\Omega}^s$ is the fluid-structure interface, see Figure 7. We denote by $\partial\Omega^f$ and $\partial\Omega^s$ the boundaries of the fluid and solid domains, respectively, and we define $\Gamma^f = \partial\Omega^f \setminus \Sigma$

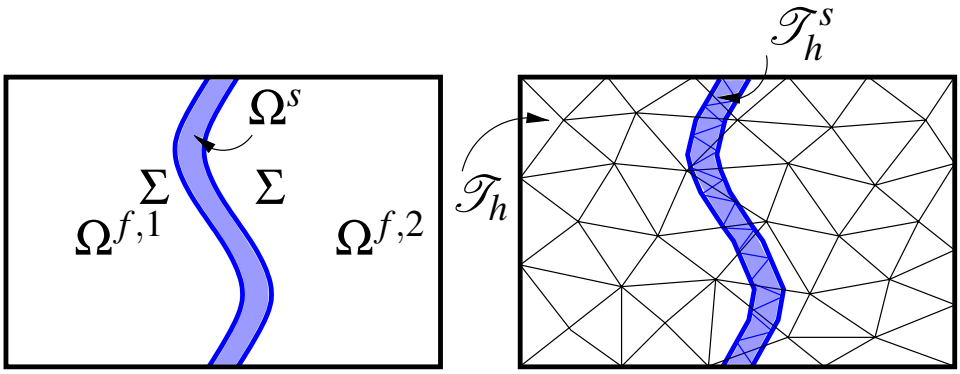

Figure 6: Left: the background domain is overlapped by a thin foreground domain Ω^s. The interface Σ separates the fluid background process domains ($\Omega^{f,1}$ and $\Omega^{f,2}$) to the solid foreground domain. Right: The solid foreground mesh $\mathscr{T}_h^s$ overlaps the background mesh $\mathscr{T}_h$ that covers the entire domain. The thickness of $\mathscr{T}_h^s$ is smaller than the size of the background mesh elements.

and $\Gamma^s = \partial\Omega^s \setminus \Sigma$. Finally, we indicate by $\mathbf{n}^f$ and $\mathbf{n}^s$ the outward unit normal to the domain Ω^f and Ω^s, respectively. On the interface Σ we have $\mathbf{n}^f = -\mathbf{n}^s = \mathbf{n}$.

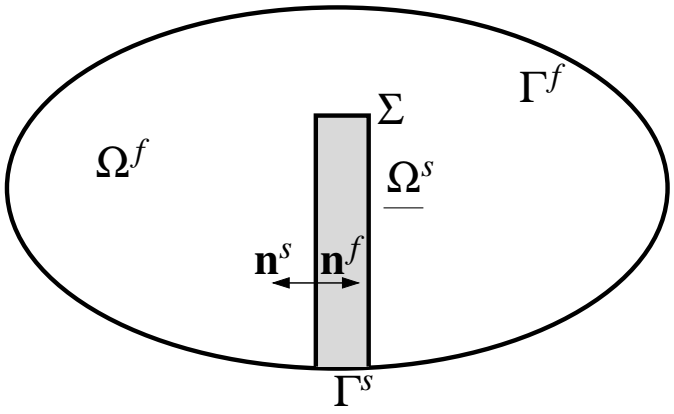

Figure 7: Sketch of the fluid and structure domain Ω^f and Ω^s with the fluid-structure interface Σ.

The continuous fluid-structure interaction problem reads as follows: Find for any $t \in (0,T]$, the fluid velocity $\mathbf{u}(t) : \Omega^f(t) \to \mathbb{R}^d$, the fluid pressure $p(t) : \Omega^f(t) \to \mathbb{R}$, the solid displacement $\widehat{\mathbf{d}}(t) : \widehat{\Omega}^s \to \mathbb{R}^d$, and the fluid domain displacement $\mathbf{d}^f(t) : \Sigma \to \mathbb{R}^d$, such that

• Fluid problem:

$$\begin{cases} \rho^f \partial_t \mathbf{u} + \rho^f \mathbf{u} \cdot \nabla \mathbf{u} - \nabla \cdot \mathbf{T}^f(\mathbf{u}, p) = \mathbf{0} & \text{in } \Omega^f(\mathbf{d}^f), \\ \nabla \cdot \mathbf{u} = 0 & \text{in } \Omega^f(\mathbf{d}^f), \\ \mathbf{u} = \mathbf{g} & \text{on } \Gamma_D^f(\mathbf{d}^f), \\ \mathbf{T}^f(\mathbf{u}, p)\mathbf{n}^f = \mathbf{h} & \text{on } \Gamma_N^f(\mathbf{d}^f); \end{cases} \tag{4}$$

• Solid problem:

$$\begin{cases} \rho^s \partial_{tt} \widehat{\mathbf{d}} - \nabla \cdot \widehat{\mathbf{T}}^s(\widehat{\mathbf{d}}) = \mathbf{0} & \text{in } \widehat{\Omega}^s, \\ \widehat{\mathbf{d}} = \mathbf{0} & \text{on } \widehat{\Gamma}^s; \end{cases} \tag{5}$$

• Coupling conditions:

$$\begin{cases} \mathbf{u} = \partial_t \mathbf{d} & \text{on } \Sigma(\mathbf{d}^f), \\ \mathbf{T}^f(\mathbf{u}, p)\mathbf{n}^f = -\mathbf{T}^s(\mathbf{d})\mathbf{n}^s & \text{on } \Sigma(\mathbf{d}^f); \end{cases} \tag{6}$$

• Geometric condition:

$$\mathbf{d}^f = \mathbf{d} \qquad \text{on } \Sigma(\mathbf{d}^f), \tag{7}$$

where (4) are the Navier-Stokes equations, (5) are the equations of elasto-dynamics, (6) are the physical coupling conditions (kinematic and dynamic, respectively), and (7) is the condition that guarantees the geometric adherence between the fluid and solid domains. We have highlighted the dependence of the fluid domain and of its boundaries on the interface displacement $\mathbf{d}_f$, which in fact couples geometrically the fluid and the structure sub-problems. We point out that the fluid problem (4) is written in an Eulerian framework, i.e. in the deformed configuration, while the solid problem (5) is written in the Lagrangian framework, i.e. in the reference configuration. We have indicated with the superscript $\widehat{\cdot}$ the quantities evaluated in the reference configuration. The quantities without $\widehat{\cdot}$ are referred to the current instant t. We have $\Gamma^f = \Gamma_D^f \cup \Gamma_N^f$ and we have considered a Dirichlet boundary condition on Γ_D^f and a Neumann condition on Γ_N^f, with $\mathbf{g}$ and $\mathbf{h}$ suitable functions with the required regularity. . Moreover, ρ^f and ρ^s are the fluid and structure densities, $\mathbf{T}^f(\mathbf{u}, p) = -p\mathbf{I} + 2\mu^f \mathbf{D}(\mathbf{u})$ is the fluid Cauchy stress tensor, with μ^f the fluid viscosity and $\mathbf{D}(\mathbf{w}) = \dfrac{\nabla \mathbf{w} + \nabla^T \mathbf{w}}{2}$, $\widehat{\mathbf{T}}^s(\widehat{\mathbf{d}})$ is the first Piola-Kirchhoff solid stress tensor. Moreover, $\widehat{\mathbf{T}}^s = J\mathbf{T}^s\mathbf{F}^{-T}$ is the formula to pass from the solid Cauchy stress tensor $\mathbf{T}^s$ to the Piola-Kirchhoff tensor, with $\mathbf{F} = \nabla \mathbf{x}$ the deformation gradient, i.e. the gradient of the coordinates in the current position with respect to the reference space coordinates, and $J = \det(\mathbf{F})$ is its determinant. For

the sake of simplicity we have considered homogeneous Dirichlet conditions on $\widehat{\Gamma}^s$. Moreover, the FSI problem given by equations (4)-(7) has to be completed with initial conditions for the fluid and solid velocity and displacement.

The mechanical behaviour is described by a second order exponential model defined by the following the strain energy function:

$$\mathscr{W}(I_1) = \frac{\kappa}{4}\Big((J-1)^2 + ln^2(J)\Big) + \frac{\alpha}{2\gamma}\Big(e^{\gamma(I_1-3)^2} - 1\Big), \tag{8}$$

where $I_1 = tr(\mathbf{C})$, $\mathbf{C} = \mathbf{F}^T\mathbf{F}$ is the right Cauchy-Green tensor, α is the shear modulus that represents the mechanical stiffness of the material, κ is the bulk modulus and γ is a positive parameter that represents the level of non-linearity of the mechanical response of the body. The corresponding first Piola-Kirchhoff solid stress tensor reads as follows:

$$\begin{aligned}\widehat{\mathbf{T}}^s(\mathbf{F}) =& \frac{\kappa}{2}\big(J^2 - J - ln(J)\big)\,\mathbf{F}^{-T} \\ &+ 2\alpha\left(J^{-2/3}I_1 - 3\right)e^{\gamma\left(J^{-2/3}I_1-3\right)^2}J^{-2/3}\left(\mathbf{F} - \frac{1}{3}I_1\mathbf{F}^{-T}\right).\end{aligned}$$

In what follows, with the aim of writing the Extended Finite Elements/Discontinuous Galerkin (XFEM/DG) discrete formulation, we follow [95] and we introduce the meshes and the numerical spaces. To ease the presentation, we assume that Ω^f, Ω^s and Σ are polyhedral. Referring to the notation of Sect. 3, we denote by $\mathscr{T}_h^F = \mathscr{T}_h^s$ the solid foreground mesh that covers the domain Ω^s and is fitted to $\partial\Omega^s$, and by $\mathscr{T}_h$ the background mesh that covers the whole domain Ω and is fitted to Γ^f, but in general not to Σ and Γ^s. We indicate by $h > 0$ the space discretization parameter, which is a function that may vary among the elements K of the meshes and between the background and foreground meshes. As a result, the solid foreground mesh $\mathscr{T}_h^s$ overlaps the background mesh $\mathscr{T}_h$, see Figure 8 (left). Then, accordingly to definition (1), we denote by $\mathscr{T}_h^{BP} = \mathscr{T}_h^f$ the fluid background process mesh, i.e. the mesh generated by considering the restriction of $\mathscr{T}_h$ to Ω^f, defined as

$$\mathscr{T}_h^f = \{K : K = K'_{|\Omega^f}, \forall K' \in \mathscr{T}_h\}.$$

In the case of a thin foreground structure, the elements of the background mesh $\mathscr{T}_h$ could be cut by the foreground mesh and divided into several disconnected polyhedra, with a portion of the background elements overlapped by the foreground mesh, see Figure 8. We refer to these elements as *split elements*.

We introduce the following mesh

$$\mathscr{G}_h = \{K : K \in \mathscr{T}_h,\, K \cap \Sigma \neq \emptyset,\, K \cap \Omega^f \text{ is a non-connected set}\},$$

that consists of all the elements K in $\mathscr{T}_h$ cut by the interface Σ which are split elements, see Figure 9 (left). This means that each element $K \in \mathscr{G}_h$ is split into $N^K \geq 2$ fluid subparts, which in general are polyhedra. We denote by P_i^K, $i = 1, \ldots, N^K$, the polyhedra of

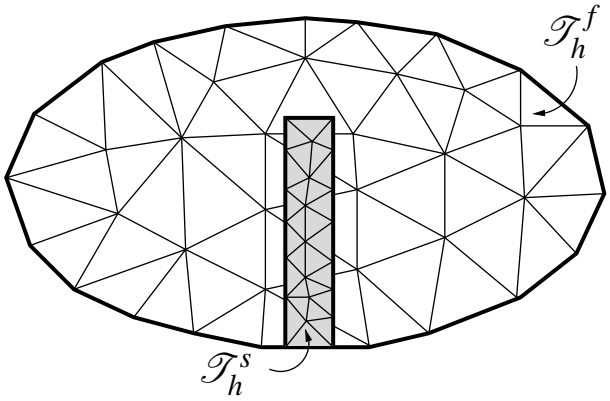

Figure 8: Left: the structure foreground mesh $\mathscr{T}_h^s$ overlaps the background mesh $\mathscr{T}_h$. Right: representation of a background element split into three disconnected polyhedra (in blue/dark) by the solid foreground mesh (in grey/light).

a split element K. We define by $\mathscr{G}_h^P$ the union of all such polyhedra P_i^K, for $i = 1, \ldots, N^K$ and for each $K \in \mathscr{G}_h$, see Figure 9 (right) where $N^K = 2$. More precisely

$$P \in \mathscr{G}_h^P \quad \longleftrightarrow \quad \exists K \in \mathscr{G}_h \text{ s.t. } P \subset K \cap \Omega^f \text{ is a connected set.}$$

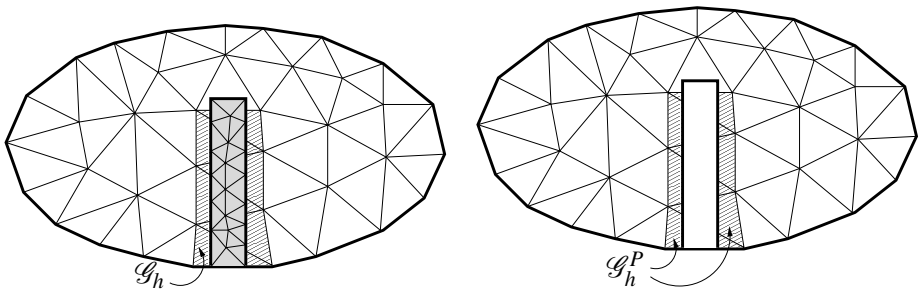

Figure 9: Left: representation of the mesh $\mathscr{G}_h$. Notice that $\mathscr{G}_h$ contains also the portion of the elements overlapped by the structure. Right: representation of the non-connected mesh $\mathscr{G}_h^P$.

The set $\mathscr{G}_h^P$ in now partitioned into its $N^f = \max_K N^K$ connected subsets $\Omega_h^{f,i}$. For example, by considering the same configuration in Figure 10 (left), we have $N^f = 2$ connected subregions ($\Omega_h^{f,1}$ and $\Omega_h^{f,2}$).

Moving from these definitions, we set

$$\Omega_h^{f,0} = \Omega^f \setminus \bigcup_{K \in \mathscr{G}_h} K.$$

Notice that $\Omega^f = \bigcup_{i=0,\ldots,N^f} \Omega_h^{f,i}$ and that $\Omega_h^{f,i} \cap \Omega_h^{f,j} = \emptyset, \forall i \neq j$. We denote by $\mathscr{T}_h^{f,0}$ the smallest mesh composed of the elements $K \in \mathscr{T}_h$ that covers the set $\Omega_h^{f,0}$, i.e.

$$K \in \mathscr{T}_h^{f,0} \quad \longleftrightarrow \quad K \cap \overline{\Omega}_h^{f,0} \neq \emptyset.$$

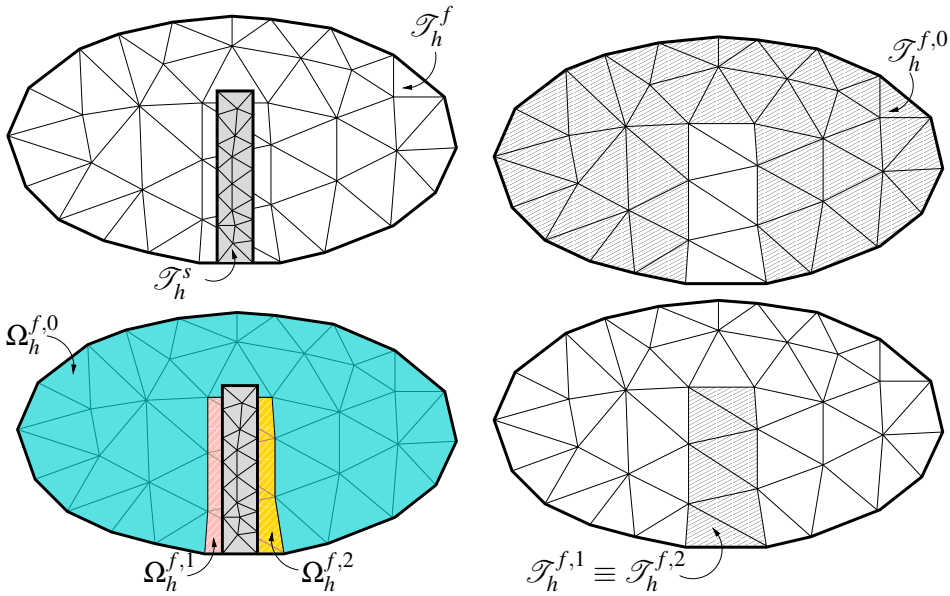

Figure 10: Left: sketch of the background ($\mathscr{T}_h$) and foreground ($\mathscr{T}_h^s$) meshes (top) and the sets $\Omega_h^{f,0}$ (blue), $\Omega_h^{f,1}$ (pink) and $\Omega_h^{f,2}$ (yellow) (bottom). Right: the shaded regions represent the meshes $\mathscr{T}_h^{f,0}$ (top) and $\mathscr{T}_h^{f,i}$ (bottom).

Finally, we denote by $\mathscr{T}_h^{f,i}$, for $i = 1,\dots,N^f$, the smallest mesh that consists of all the elements of $\mathscr{G}_h$ that covers the set $\Omega_h^{f,i}$, i.e.

$$K \in \mathscr{T}_h^{f,i} \quad \longleftrightarrow \quad K \cap \overline{\Omega}_h^{f,i} \neq \emptyset, \quad i = 1,\dots,N^f.$$

Thus, each element $K \in \mathscr{G}_h$ belongs to N^K different meshes $\mathscr{T}_h^{f,i}$, and this will allow us to duplicate the dofs of K N^K times. The idea is to build the classical FEM approximation in $\mathscr{T}_h^{f,0}$, i.e. by using the classical dofs and shape functions, and to employ the XFEM strategy in $\mathscr{T}_h^{f,i}$, $i = 1,\dots,N^f$, so that the dofs associated with the elements in $\mathscr{T}_h^{f,i}$, $i = 1,\dots,N^f$, are duplicated: a set of dofs is used to compute the solution over each mesh $\mathscr{T}_h^{f,i}$.

The unfitted nature of the fluid and solid meshes requires a specific treatment of the coupling conditions between the corresponding fluid and solid problems at the interface Σ. A possibility, considered here, is to employ a Discontinuous Galerkin (DG) mortaring, see, e.g., [23, 25], in order to weakly impose the continuity of the fluid solution between the elements of the meshes $\mathscr{T}_h^{f,i}$, $i = 1,\dots,N^f$, see below. On the contrary, in $\mathscr{T}_h^{f,0}$ it is possible to use either a non-conforming or a conforming discretization. For the sake of simplicity, we consider a conforming discretization, thus we impose a strong continuity in $\mathscr{T}_h^{f,0}$. We also notice that some operators of the discrete formulation will act on the domains $\Omega_h^{f,i} \subset \Omega^f$, while other operators, such as the stabilization terms, will act on the meshes $\mathscr{T}_h^{f,i}$, as we explain later on.

We observe that the set covered by $\mathscr{T}_h^{f,i}$ is larger than the one covered by the corresponding $\Omega_h^{f,i}$, see Figure 10 (right) for the case $N^f = 2$. More complex configurations may happen for realistic three-dimensional domains.

Remark 4.1 *We point out that the elements of the background mesh crossed by the interface Σ may be arbitrarily small due to the overlapping of the foreground domain. This may generate instabilities in the numerical solution and lead to an ill-conditioned matrix. For these reasons, to prevent instabilities and to maintain the robustness of the method, a possible strategy consists in the introduction of the ghost-penalty stabilization, see below and [21].*

We classify the faces involved in the discrete formulation as follows:

- the faces belonging to the fluid-structure interface Σ, where we impose weakly the continuity of the velocity and stresses by means of the DG formulation, see, e.g., [23, 25];
- $\mathscr{F}_{h,p}^{f,i}$, the faces in $\mathscr{T}_h^{f,i}$, $i = 1,\dots,N^f$, that belong to the background process domain Ω^f, where we impose weakly the continuity of the fluid velocity and stresses by means of the DG formulation, see below and, e.g., [6, 28];
- $\mathscr{F}_{h,\Sigma}^{f,i}$, the faces of $\mathscr{T}_h^{f,i}$, $i = 1,\dots,N^f$, cut by the interface Σ, where the *ghost penalty* stabilization term (10) is applied, see below and [21].

For a representation of these faces, we refer to Figure 11.

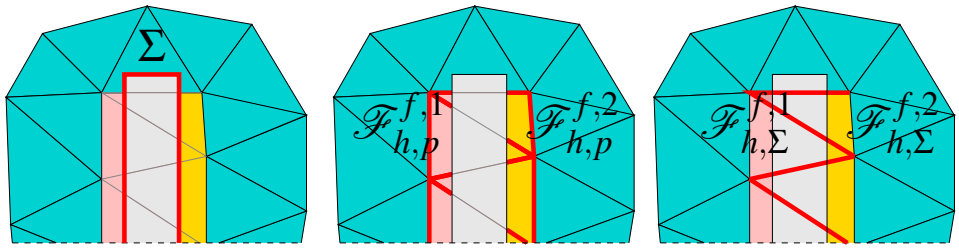

Figure 11: Representation of the sets of faces involved in the discrete formulation (highlighted in red): (left) faces of the interface Σ; (center) faces $\mathscr{F}_{h,p}^{f,1}$ and $\mathscr{F}_{h,p}^{f,2}$ for the mortaring in the background process domain; (right) faces $\mathscr{F}_{h,\Sigma}^{f,1}$ and $\mathscr{F}_{h,\Sigma}^{f,2}$ for the ghost penalty stabilization.

After a suitable time discretization of the FSI problem (4)-(5)- (6)-(7), we denote by $\Omega^{f,n}$ the approximation of Ω^f at time t^n. The discrete spaces for the fluid velocity and pressure read as follows:

$$\mathbf{V}_h^n = \{\mathbf{v}_h \in [X_h^{f,n}]^d : \mathbf{v}_{h|\Gamma^f} = \mathbf{0}\}, \quad Q_h^n = \{q_h \in X_h^{f,n}\},$$
$$\mathbf{W}_h = \{\mathbf{w}_h \in [X_h^s]^d : \mathbf{w}_{h|\Gamma^s} = \mathbf{0}\},$$

where

$$X_h^{f,n} = \{v_h \in L^2(\Omega^{f,n}) : v_h \in \mathscr{C}^0(\Omega_h^{f,0,n}), v_{h|K} \in \mathbb{P}_1(K), \\ \forall K \in \mathscr{T}_h^{f,i,n} \text{ for } i = 0, \dots, N^f\},$$

and

$$X_h^s = \{v_h \in \mathscr{C}^0(\widehat{\Omega}^s) : v_{h|K} \in \mathbb{P}_1(K), \forall K \in \mathscr{T}_h^s\}.$$

To write the discrete formulation, we introduce the trace operators defined over an interface $\mathscr{I}$ that separates a generic domain $\Omega_{1,2}$ into Ω_1 and Ω_2. For a (scalar or vectorial) function q, we denote by $[\![\cdot]\!]_{\mathscr{I}}$ the jump and by $\{\{\cdot\}\}_{\mathscr{I},\varepsilon}$ the ε-weighted mean across the interface $\mathscr{I}$, defined as

$$[\![q]\!]_{\mathscr{I}} = q_1 - q_2, \quad \{\{q\}\}_{\mathscr{I},\varepsilon} = \varepsilon q_1 + (1-\varepsilon) q_2, \tag{9}$$

where q_1 and q_2 are the traces of q at the two sides of the interface and $\varepsilon \in [0,1]$. If the subscript ε is not indicated, we assume that $\varepsilon = \frac{1}{2}$.

We consider a DG mortaring on Σ to impose the coupling conditions (6) and on the faces $\mathscr{F}_{h,p}^{f,i}$ to impose the continuity of the background fluid solution, by mimicking the (symmetric) interior penalty method, introduced for example in [6, 31] for the Poisson problem. Moreover, a ghost penalty term, see [21], is applied on $\mathscr{F}_{h,\Sigma}^{f,i}$ to guarantee robustness of the method with respect to the elements crossed by the interface Σ, defined as

$$g_h(\mathbf{u}_h, \mathbf{v}_h) = \gamma_g \sum_{i=1}^{N^f} \sum_{F \in \mathscr{F}_{h,\Sigma}^{f,i}} \mu^f h_F \int_F [\![\nabla \mathbf{u}_h]\!]_F \, \mathbf{n} \cdot [\![\nabla \mathbf{v}_h]\!]_F \, \mathbf{n}, \tag{10}$$

with $\gamma_g > 0$;

We also introduce a stabilizing term s_h to handle spurious pressure and velocity instabilities due to equal order Finite Elements and to dominating convection regimes, respectively. In this work we considered the *interior penalty* (IP) stabilization, see [24], as done in [82].

We now introduce the following forms.

- Fluid form collecting the classical Navier-Stokes terms and the ghost and IP stabilizations:

$$\begin{aligned} \mathscr{A}^f(\mathbf{z}, \mathbf{u}, p; \mathbf{v}, q)^r = & \frac{\rho^f}{\Delta t}(\mathbf{u}, \mathbf{v})_{\Omega^{f,r}} + 2\mu^f(\mathbf{D}(\mathbf{u}), \mathbf{D}(\mathbf{v}))_{\Omega^{f,r}} \\ & - (p, \nabla \cdot \mathbf{v})_{\Omega^{f,r}} + (q, \nabla \cdot \mathbf{u})_{\Omega^{f,r}} + \rho^f(\mathbf{z} \cdot \nabla \mathbf{u}, \mathbf{v})_{\Omega^{f,r}} \\ & + s_h(\mathbf{u}, p; \mathbf{v}, q)^r + g_h(\mathbf{u}, \mathbf{v})^r; \end{aligned}$$

- Structure form:

$$\mathscr{A}^s\left(\widehat{\mathbf{d}}; \widehat{\mathbf{w}}\right) = \frac{\rho^s}{\Delta t^2}(\widehat{\mathbf{d}}, \widehat{\mathbf{w}})_{\widehat{\Omega}^s} + (\widehat{\mathbf{T}}^s(\widehat{\mathbf{d}}), \nabla \widehat{\mathbf{w}})_{\widehat{\Omega}^s};$$

- Form related to the DG terms involving only the fluid unknowns and test functions:

$$\begin{aligned}\mathscr{D}^{ff}(\mathbf{u},p;\mathbf{v},q)^r = &-\sum_{i=1}^{N^f}\sum_{F\in\mathscr{F}_{h,p}^{f,i,r}}\left(\left\{\left\{\mathbf{T}^f(\mathbf{u},p)\right\}\right\}_F\mathbf{n},[\![\mathbf{v}]\!]_F\right)_F\\ &-\sum_{i=1}^{N^f}\sum_{F\in\mathscr{F}_{h,p}^{f,i,r}}\left([\![\mathbf{u}]\!]_F,\left\{\left\{\mathbf{T}^f(\mathbf{v},-q)\right\}\right\}_F\mathbf{n}\right)_F\\ &+\sum_{i=1}^{N^f}\sum_{F\in\mathscr{F}_{h,p}^{f,i,r}}\frac{\gamma_p\mu^f}{h_F}([\![\mathbf{u}]\!]_F,[\![\mathbf{v}]\!]_F)_F,\\ &-\left(\varepsilon\mathbf{T}^f(\mathbf{u},p)\mathbf{n},\mathbf{v}\right)_{\Sigma^r}-\left(\mathbf{u},\varepsilon\mathbf{T}^f(\mathbf{v},-q)\mathbf{n}\right)_{\Sigma^r}+\frac{\gamma_\Sigma\mu^f}{h}(\mathbf{u},\mathbf{v})_{\Sigma^r};\end{aligned} \tag{11}$$

- Form related to the DG terms involving only the structure unknowns and test functions:

$$\begin{aligned}\mathscr{D}^{ss}\left(\widehat{\mathbf{d}};\widehat{\mathbf{w}}\right) = &-\left((1-\varepsilon)\widehat{\mathbf{T}}^s(\widehat{\mathbf{d}})\mathbf{n},-\widehat{\mathbf{w}}\right)_{\widehat{\Sigma}}\\ &-\left(-\frac{\widehat{\mathbf{d}}}{\Delta t},(1-\varepsilon)\widehat{\mathbf{T}}^s(\widehat{\mathbf{w}})\mathbf{n}\right)_{\widehat{\Sigma}}\\ &+\frac{\gamma_\Sigma\mu^f}{h}\left(-\frac{\widehat{\mathbf{d}}}{\Delta t},-\widehat{\mathbf{w}}\right)_{\widehat{\Sigma}};\end{aligned} \tag{12}$$

- Form related to the DG terms involving mixed (fluid and structure) unknowns and test functions:

$$\begin{aligned}\mathscr{D}^{fs}(\mathbf{u},p,\mathbf{d};\mathbf{v},q,\mathbf{w})^r = &-\left(\varepsilon\mathbf{T}^f(\mathbf{u},p)\mathbf{n},-\mathbf{w}\right)_{\Sigma^r}-\left((1-\varepsilon)\mathbf{T}^s(\mathbf{d})\mathbf{n},\mathbf{v}\right)_{\Sigma^r}\\ &-(\mathbf{u},(1-\varepsilon)\mathbf{T}^s(\mathbf{w})\mathbf{n})_{\Sigma^r}-\left(-\frac{\mathbf{d}}{\Delta t},\varepsilon\mathbf{T}^f(\mathbf{v},-q)\mathbf{n}\right)_{\Sigma^r}\\ &+\frac{\gamma_\Sigma\mu^f}{h}(\mathbf{u},-\mathbf{w})_{\Sigma^r}+\frac{\gamma_\Sigma\mu^f}{h}\left(-\frac{\mathbf{d}}{\Delta t},\mathbf{v}\right)_{\Sigma^r};\end{aligned} \tag{13}$$

- Right hand side given by terms coming from time discretization and forcing terms:

$$\mathscr{F}(\mathbf{u}^m,p^m,\mathbf{d}^m;\mathbf{v},q,\mathbf{w})^r=\frac{\rho^f}{\Delta t}(\mathbf{u}^m,\mathbf{v})_{\Omega^{f,r}}+\frac{2\rho^s}{\Delta t^2}(\widehat{\mathbf{d}}^m,\widehat{\mathbf{w}})_{\widehat{\Omega}^s}-\frac{\rho^s}{\Delta t^2}(\widehat{\mathbf{d}}^{m-1},\widehat{\mathbf{w}})_{\widehat{\Omega}^s}$$
$$+\left(\frac{\mathbf{d}^m}{\Delta t},\varepsilon\mathbf{T}^f(\mathbf{v},-q)\mathbf{n}+(1-\varepsilon)\mathbf{T}^s(\mathbf{w})\mathbf{n}\right)_{\Sigma^r}$$
$$-\frac{\gamma_\Sigma\mu^f}{h}\left(\frac{\mathbf{d}^m}{\Delta t},\mathbf{v}-\mathbf{w}\right)_{\Sigma^r}+(\mathbf{f}^{f,m+1},\mathbf{v})_{\Omega^{f,r}}+(\widehat{\mathbf{f}}^{s,m+1},\widehat{\mathbf{w}})_{\widehat{\Omega}^s}.$$

Notice that the DG mortaring terms introduce two penalty parameters, $\gamma_p>0$ and $\gamma_\Sigma>0$. The first parameter appears in the term $\mathscr{D}^{ff}$ and it is related to the mortaring on the faces in $\mathscr{F}_{h,p}^{f,i,r}$, while the latter appears in terms $\mathscr{D}^{ff},\mathscr{D}^{fs},\mathscr{D}^{ss}$ and it is related to the mortaring on the fluid-structure interface Σ.

Thus, the XFEM/DG approximation of the monolithic FSI problem (4)-(5)- (6)-(7) reads: For each n, find $(\mathbf{u}_h^{n+1},p_h^{n+1},\widehat{\mathbf{d}}_h^{n+1})\in\mathbf{V}_h^{n+1}\times Q_h^{n+1}\times\mathbf{W}_h$ such that

$$\begin{aligned}&\mathscr{A}^f\left(\mathbf{u}_h^{n+1},\mathbf{u}_h^{n+1},p_h^{n+1};\mathbf{v}_h,q_h\right)^{n+1}+\mathscr{A}^s\left(\widehat{\mathbf{d}}_h^{n+1};\widehat{\mathbf{w}}_h\right)\\&+\mathscr{D}^{ff}\left(\mathbf{u}_h^{n+1},p_h^{n+1};\mathbf{v}_h,q_h\right)^{n+1}+\mathscr{D}^{ss}\left(\widehat{\mathbf{d}}_h^{n+1};\widehat{\mathbf{w}}_h\right)+\mathscr{D}^{fs}\left(\mathbf{u}_h^{n+1},p_h^{n+1},\mathbf{d}_h^{n+1};\mathbf{v}_h,q_h,\mathbf{w}_h\right)^{n+1}\\&=\mathscr{F}\left(\mathbf{u}_h^n,p_h^n,\mathbf{d}_h^n;\mathbf{v}_h,q_h,\widehat{\mathbf{w}}_h\right)^n\end{aligned}\tag{14}$$

for all $(\mathbf{v}_h,q_h,\widehat{\mathbf{w}}_h)\in\mathbf{V}_h^{n+1}\times Q_h^{n+1}\times\mathbf{W}_h$. In compact form we write

$$\mathscr{H}\left(\mathbf{u}_h^{n+1},p_h^{n+1},\widehat{\mathbf{d}}_h^{n+1};\mathbf{v}_h,q_h,\widehat{\mathbf{w}}_h\right)^{n+1}=0$$

for all $(\mathbf{v}_h,q_h,\widehat{\mathbf{w}}_h)\in\mathbf{V}_h^{n+1}\times Q_h^{n+1}\times\mathbf{W}_h$

Remark 4.2 *Notice that in the previous formulation we could consider also a correction in the trilinear form to maintain the condition that the latter vanishes for* $\mathbf{z}=\mathbf{u}$ *at the discrete level [28, 84] and a term to maintain the consistency of the formulation [95]. This is what we did in the numerical experiments. However, to simplify the notation and focus on the XFEM/DG discretization, we omitted these terms in* (14).

5 An inexact-Newton method for the solution of the FSI problem

For the solution of the FSI problem (14), we introduce in what follows an inexact Newton-Krylov method, used in combination with a block Gauss-Seidel preconditioner.

To this aim, we indicate by $\delta y_{(k)}=y_{(k)}-y_{(k-1)}$ the increment of a quantity y and we consider the following linearized forms:

-

$$\widetilde{\mathscr{A}^s}\left(\delta\widehat{\mathbf{d}}_{(k)};\widehat{\mathbf{w}}\right)=\frac{\rho^s}{\Delta t^2}\left(\delta\widehat{\mathbf{d}}_{(k)},\widehat{\mathbf{w}}\right)_{\widehat{\Omega}^s}+\left(D_F\widehat{\mathbf{T}}^s(\widehat{\mathbf{d}}_{(k-1)}):\delta\widehat{\mathbf{d}}_{(k)},\nabla\widehat{\mathbf{w}}\right)_{\widehat{\Omega}^s},$$

where D_F indicated the Gateaux derivative with respect to $\mathbf{F}$;

-

$$\begin{aligned}\widetilde{\mathscr{D}}^{ss}\left(\delta\widehat{\mathbf{d}}_{(k)};\widehat{\mathbf{w}}\right)=&-\left(\left((1-\varepsilon)D_F\widehat{\mathbf{T}}^s(\widehat{\mathbf{d}}_{(k-1)}):\delta\widehat{\mathbf{d}}_{(k)}\right)\mathbf{n},-\widehat{\mathbf{w}}\right)_{\widehat{\Sigma}}\\&-\left(-\frac{\delta\widehat{\mathbf{d}}_{(k)}}{\Delta t},\left((1-\varepsilon)D_F\widehat{\mathbf{T}}^s(\widehat{\mathbf{d}}_{(k-1)}):\nabla\widehat{\mathbf{w}}\right)\mathbf{n}\right)_{\widehat{\Sigma}}\\&+\frac{\gamma_\Sigma\mu^f}{h}\left(-\frac{\delta\widehat{\mathbf{d}}_{(k)}}{\Delta t},-\widehat{\mathbf{w}}\right)_{\widehat{\Sigma}};\end{aligned}$$

-

$$\begin{aligned}\widetilde{\mathscr{D}}^{fs}\left(\mathbf{u}_{(k)},p_{(k)},\delta\mathbf{d}_{(k)};\mathbf{v},q,\mathbf{w}\right)^r=&-\left(\varepsilon\mathbf{T}^f(\mathbf{u}_{(k)},p_{(k)})\mathbf{n},-\mathbf{w}\right)_{\Sigma^r}\\&-\left(\left((1-\varepsilon)D_F\mathbf{T}^s(\mathbf{d}_{(k-1)}):\nabla\delta\mathbf{d}_{(k)}\right)\mathbf{n},\mathbf{v}\right)_{\Sigma^r}\\&-\left(\mathbf{u}_{(k)},\left((1-\varepsilon)D_F\mathbf{T}^s(\mathbf{d}^m_{(k-1)}):\nabla\mathbf{w}\right)\mathbf{n}\right)_{\Sigma^r}\\&-\left(-\frac{\delta\mathbf{d}_{(k)}}{\Delta t},\varepsilon\mathbf{T}^f(\mathbf{v},-q)\mathbf{n}\right)_{\Sigma^r}\\&+\frac{\gamma_\Sigma\mu^f}{h}\left(\mathbf{u}_{(k)},-\mathbf{w}\right)_{\Sigma^r}+\frac{\gamma_\Sigma\mu^f}{h}\left(-\frac{\delta\mathbf{d}_{(k)}}{\Delta t},\mathbf{v}\right)_{\Sigma^r}.\end{aligned}$$

Moreover, we consider the approximated form $\widetilde{\widetilde{\mathscr{D}}}^{fs}$ instead of $\widetilde{\mathscr{D}}^{fs}$ obtained by considering the following approximation

$$\frac{\partial\mathbf{T}^s}{\partial\mathbf{F}}=\frac{\partial}{\partial\mathbf{F}}(J^{-1}\widehat{\mathbf{T}}^s\mathbf{F}^T)\;\approx\;J^{-1}\frac{\partial\widehat{\mathbf{T}}^s}{\partial\mathbf{F}}\mathbf{F}^T.$$

This, together with the fixed point iteration strategy (instead of the full Newton method) used for the fluid problem (see (15)) leads to an inexact Newton method.

Finally, we point out that at each iteration of the inexact Newton method, we have to update the fluid mesh obtained by the intersections generated by the moving structure mesh onto the background fixed one (see Figure 4), and, accordingly, the velocity and pressure spaces. In particular, we introduce the compact notation *updatedDomainsAndSpaces()* that at time t^{n+1}, iteration k, performs the following steps:

1. given the displacement at the previous iteration $\widehat{\mathbf{d}}^{n+1}_{h,(k-1)}$, computation of the new position of the solid mesh $(\mathscr{T}^s_h)^{n+1}_{(k-1)}$;

2. computation of the new fluid mesh $(\mathscr{T}_h^f)_{(k-1)}^{n+1}$. This is done by intersecting the background mesh $\mathscr{T}_h$ and the solid mesh $(\mathscr{T}_h^s)_{(k-1)}^{n+1}$;

3. definition of the new discrete spaces $\mathbf{V}_{h,(k-1)}^{n+1}$ and $Q_{h,(k-1)}^{n+1}$.

The FSI problem (14) is solved by means of the following algorithm:

Algorithm 1 Inexact Newton method for the FSI problem (14)

At time t^{n+1}, given an initial solution $\mathbf{u}_{h,(0)}^{n+1}$, $p_{h,(0)}^{n+1}$, $\widehat{\mathbf{d}}_{h,(0)}^{n+1}$:
for $k = 1 : k_{max}$ **do**

1. *updateDomainsAndSpaces()*;

2. Find $(\mathbf{u}_{h,(k)}^{n+1}, p_{h,(k)}^{n+1}, \delta\widehat{\mathbf{d}}_{h,(k)}^{n+1}) \in \mathbf{V}_{h,(k-1)}^{n+1} \times Q_{h,(k-1)}^{n+1} \times \mathbf{W}_h$ such that

$$\begin{aligned}
&\mathscr{A}^f\left(\mathbf{u}_{h,(k-1)}^{n+1}, \mathbf{u}_{h,(k)}^{n+1}, p_{h,(k)}^{n+1}; \mathbf{v}_h, q_h\right)_{(k-1)}^{n+1} + \widetilde{\mathscr{A}^s}\left(\delta\widehat{\mathbf{d}}_{h,(k)}^{n+1}; \widehat{\mathbf{w}}_h\right) \\
&+\mathscr{D}^{ff}\left(\mathbf{u}_{h,(k)}^{n+1}, p_{h,(k)}^{n+1}; \mathbf{v}_h, q_h\right)_{(k-1)}^{n+1} + \widetilde{\mathscr{D}}^{ss}\left(\delta\widehat{\mathbf{d}}_{h,(k)}^{n+1}; \widehat{\mathbf{w}}_h\right) \\
&+\widehat{\widetilde{\mathscr{D}}}^{fs}\left(\mathbf{u}_{h,(k)}^{n+1}, p_{h,(k)}^{n+1}, \delta\mathbf{d}_{h,(k)}^{n+1}; \mathbf{v}_h, q_h, \mathbf{w}_h\right)_{(k-1)}^{n+1} \\
&= -\mathscr{H}\left(\mathbf{u}_{h,(k-1)}^{n+1}, p_{h,(k-1)}^{n+1}, \mathbf{d}_{h,(k-1)}^{n+1}; \mathbf{v}_h, q_h, \widehat{\mathbf{w}}_h\right)_{(k-1)}^{n+1},
\end{aligned} \tag{15}$$

   for all $(\mathbf{v}_h, q_h, \widehat{\mathbf{w}}_h) \in \mathbf{V}_{h,(k-1)}^{n+1} \times Q_{h,(k-1)}^{n+1} \times \mathbf{W}_h$;

3. $\widehat{\mathbf{d}}_{h,(k)}^{n+1} = \widehat{\mathbf{d}}_{h,(k-1)}^{n+1} + \delta\widehat{\mathbf{d}}_{h,(k)}^{n+1}$.

end for

Remark 5.1 *Notice that in this case, due to the fixed nature of the background mesh, we do not have any geometric problem, thus no shape derivatives appear in the exact Jacobian.*

6 Numerical results

In this section, we present some numerical results for the FSI problem given by equations (4)-(7). We consider Algorithm 1 for its numerical solution. We present the following test cases:

- *Blocked channel*: A time-dependent FSI problem with an immersed non-linear elastic structure that completely blocks a channel;
- *Non-linear elastic slab*: A time-dependent FSI problem with an immersed non-linear elastic slab with a high Reynolds number;
- *Ideal aortic valve*: A time-dependent FSI problem in the case of three immersed linear elastic leaflets.

The proposed examples are simulated in a three-dimensional (3D) framework, and for the structure we use the non-linear strain energy function (8) for the blocked channel and non-linear elastic slab tests, whereas the Hooke law for the ideal aortic valve. The mortaring parameter ε for the fluid-solid coupling in the forms $\mathscr{D}^{ff}$, $\mathscr{D}^{fs}$, $\mathscr{D}^{ss}$ and in functional $\mathscr{F}$ is set equal to 1, see [23]. Moreover, we point out that at iteration k of Algorithm 1, the fluid velocity $\mathbf{u}_h^n$ at the previous time step appearing in the term coming from time discretization (which is defined in $\Omega^{f,n}$) and the fluid velocity $\mathbf{u}_{h,(k-1)}^{n+1}$ at the previous iteration used in the convective term (which is defined in $\Omega_{(k-2)}^{f,n+1}$) are not defined in the current domain $\Omega_{(k-1)}^{f,n+1}$ (remember that at iteration k the fluid problem is solved in $\Omega_{(k-1)}^{f,n+1}$). Thus, these terms should be properly defined in the new computational domain $\Omega_{(k-1)}^{f,n+1}$ in order to be used in the discrete formulation. In particular, issues may occur when the uncovered portion of a fluid element change between time n and $n+1$ and/or between iteration $k-1$ and k. For the numerical treatment of these cases, we employ the procedure proposed in [95].

The simulations have been performed with the Finite Element library LifeV [1].

6.1 Blocked channel

In this experiment we consider a thick membrane placed in the middle of a channel so that the structure completely blocks the flow in the channel, see Figure 12. The aim of this example is to assess the validity of the proposed method. We consider a background domain $\Omega = 0.4\,cm \times 0.2\,cm \times 0.00625\,cm$ and a structure domain $\Omega^s = 0.01\,cm \times 0.2\,cm \times 0.00625\,cm$. The resulting fluid domain is $\Omega^f = \Omega \setminus \Omega^s$. Notice that, to ease the computational cost, we reduce the size of the domain along the z-axis. We impose $\mathbf{T}^f\mathbf{n} = (-1000,0,0)\,dyne/cm^2$ at the inlet Γ_{in}, $\mathbf{T}^f\mathbf{n} = \mathbf{0}$ at the outlet Γ_{out}, $\mathbf{u} = \mathbf{0}$ on Γ_{wall}^f, and $\mathbf{u}\cdot\widehat{\mathbf{k}} = 0$, $(\mathbf{T}^f\mathbf{n})\cdot\widehat{\mathbf{l}} = 0, \mathbf{l} = \{\mathbf{i},\mathbf{j}\}$, on the remaining portions of the fluid boundary, i.e. for $z = \{0, 0.00625\}$. Notice that the latter choice allows the fluid to move in the xy-plane at the extreme surfaces $z = \{0, 0.00625\}$. The solid is fixed at Γ_{wall}^s, i.e. $\mathbf{d} = \mathbf{0}$, and, like the fluid, is allowed to move in the xy-plane on the remaining portions of the boundary, i.e. $\mathbf{d}\cdot\widehat{\mathbf{k}} = 0$, $(\mathbf{T}^s\mathbf{n})\cdot\widehat{\mathbf{l}} = 0, \mathbf{l} = \{\mathbf{i},\mathbf{j}\}$, for $z = \{0, 0.00625\}$. As initial conditions, we set $\mathbf{u}(\mathbf{x},0) = \mathbf{d}(\mathbf{x},0) = \dot{\mathbf{d}}(\mathbf{x},0) = \mathbf{0}$. We also use the following values for the parameters: $\rho^f = 1\,g/cm^3$, $\rho^s = 1.2\,g/cm^3$, $\mu^f = 0.035\,poise$, $\alpha = 1\cdot 10^8\,dyne/cm^2$, $\kappa = 1.034\cdot 10^7\,dyne/cm^2$, $\gamma = 1$, and $T = 0.02\,s$.

We employ a background mesh $\mathscr{T}_h$ composed of $16\cdot 10^3$ tetrahedra ($h_{ave} = 0.00571\,cm$) and a solid mesh $\mathscr{T}_h^s$ composed of $1.4\cdot 10^3$ tetrahedra ($h_{ave} = 0.00377\,cm$). Notice that, the thickness of the structure domain ($0.01\,cm$) is higher than the average size of the fluid elements, so that we are in the thick case. The time step Δt is $2\cdot 10^{-4}\,s$. We choose $\gamma_\Sigma = 10^4$ (see equations (11)-(13)), $\gamma_p = 10^3$ (see equation (11)) and $\gamma_g = 1$ (see equation (10)).

In Figure 13 and 14, we show the numerical solution at different time steps. In particular, we plot the velocity and the pressure fields in the fluid domain and the structure displacement in the solid domain. A quantitative plot of the displacement of the center of mass of the structure is reported in Figure 15.

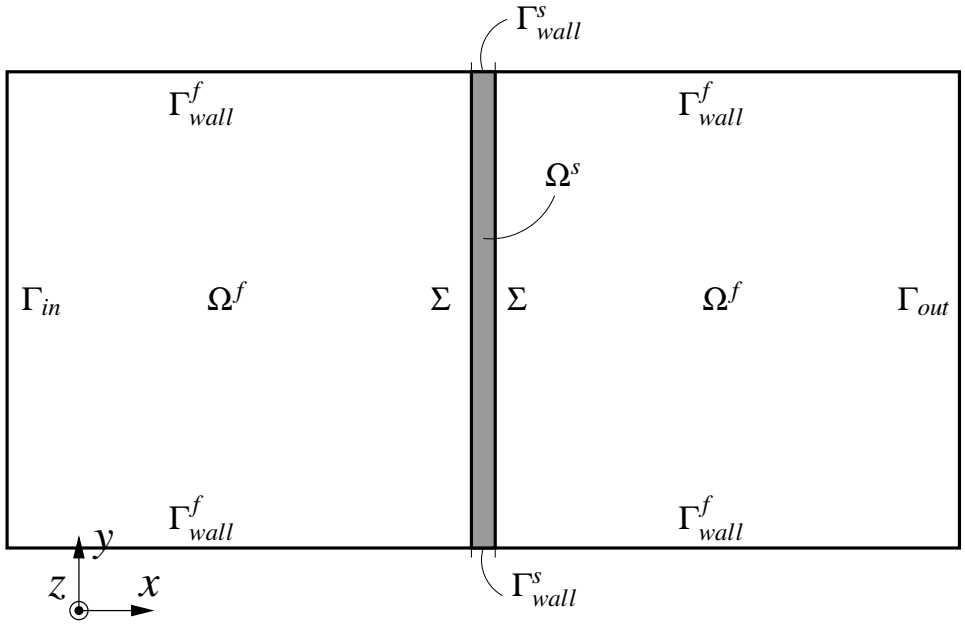

Figure 12: Top view of the fluid Ω^f and structure Ω^s domains. Blocking channel test.

Finally, in Figure 16 (left), we plot the behaviour in time of the total amount of fluid (in cm^3) that goes through Γ_{in} (indicated by V_{in}) and Γ_{out} (indicated by V_{out}), the variation of the structure volume (in cm^3) with respect to the initial time (indicated by ΔV^s), and the sum of these three quantities (indicated by $V_{balance}$) which represents the error with respect to the balance of volume. In Figure 16 (right), we plot relative error of the balance of volume, i.e. the ratio $r = V_{balance}/V^f_{eff}$, where V^f_{eff} is the effective volume available for the fluid. We see that the error committed by the method is very small compared to the total amount of volume.

6.2 Non-linear elastic slab

We consider a background domain $\Omega = (0,0.5)^3\, cm$ and a structure domain $\Omega^s = (0.025,0.425)\, cm \times (0.15,0.35)\, cm \times (0.10,0.13)\, cm$, so that the fluid domain is $\Omega^f = \Omega \setminus \overline{\Omega}^s$, see Figure 17. We impose $\mathbf{u} = (0,0,100)\, cm/s$ at the inlet Γ_{in}, $\mathbf{T}^f\mathbf{n} = \mathbf{0}$ at the outlet Γ_{out}, $\mathbf{u}\cdot\widehat{\mathbf{i}} = 0$, $(\mathbf{T}^f\mathbf{n})\cdot\widehat{\mathbf{l}} = 0, \mathbf{l} = \{\mathbf{j},\mathbf{k}\}$, at Γ_{symm}, and $\mathbf{u} = \mathbf{0}$ on the remaining portions of the fluid boundary. The structure is fixed at $x = 0.025\, cm$, i.e. $\mathbf{d} = \mathbf{0}$ at Γ^s_{wall}. The fluid-structure interface is given by $\Sigma = \partial\Omega^s \setminus \Gamma^s_{wall}$. As initial conditions, we set $\mathbf{u}(\mathbf{x},0) = \mathbf{d}(\mathbf{x},0) = \dot{\mathbf{d}}(\mathbf{x},0) = \mathbf{0}$. We also use the following values for the parameters: $\rho^f = 1\, g/cm^3$, $\rho^s = 1.2\, g/cm^3$, $\mu^f = 0.035\, poise$, $\alpha = 1.667 \cdot 10^8\, dyne/cm^2$, $\kappa = 1.724 \cdot 10^7\, dyne/cm^2$, $\gamma = 1$, and $T = 0.015 \cdot 10^{-3}\, s$. The Reynolds number is equal to $Re = 1400$.

We employ a background mesh $\mathscr{T}_h$ composed of $56 \cdot 10^3$ tetrahedra ($h_{ave} = 0.025\, cm$) and a solid mesh $\mathscr{T}^s_h$ composed of $30 \cdot 10^3$ tetrahedra ($h_{ave} = 0.0078\, cm$). Notice that, the thickness of the structure domain ($0.03\, cm$) is comparable to the average size of the

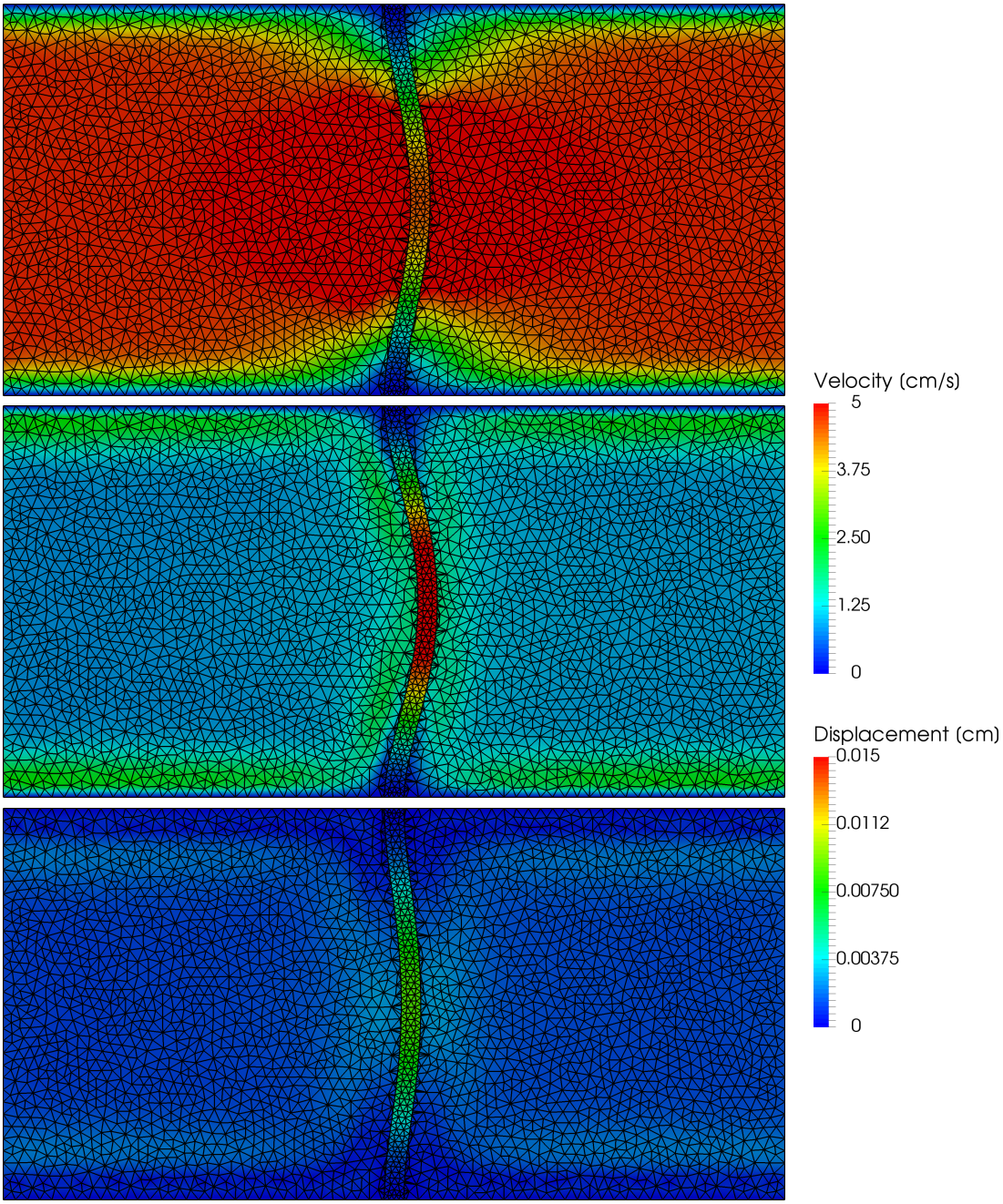

Figure 13: Plot of the fluid velocity magnitude (in cm/s) and structure displacement magnitude (in cm) at different time steps. Top: $t = 0.0026\,s$. Center: $t = 0.0040\,s$. Bottom: $t = 0.0066\,s$. Blocking channel test.

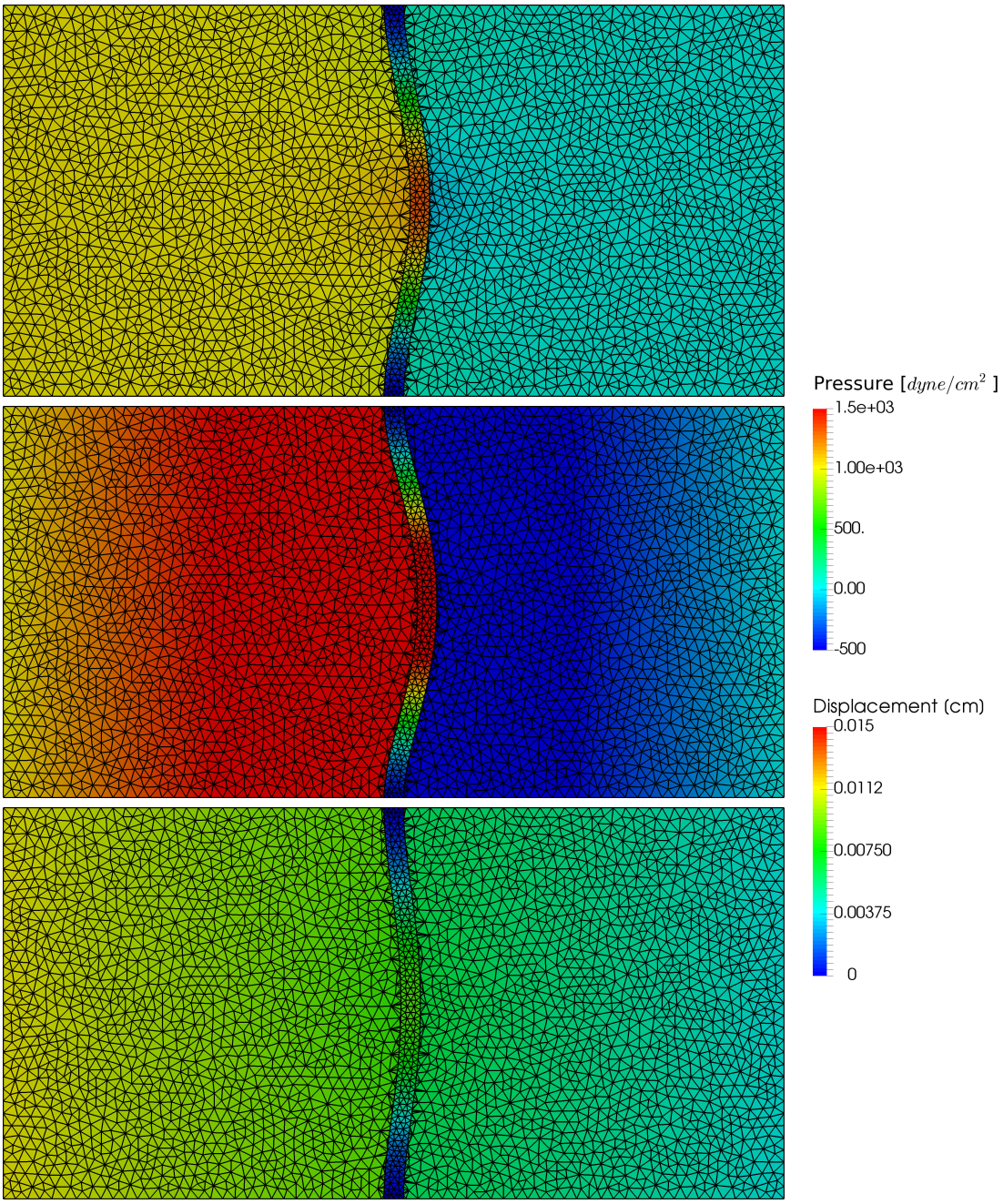

Figure 14: Plot of the fluid pressure filed (in $dyne/cm^2$) and structure displacement magnitude (in cm) at different time steps. Top: $t = 0.0026\,s$. Center: $t = 0.0040\,s$. Bottom: $t = 0.0066\,s$. Blocking channel test.

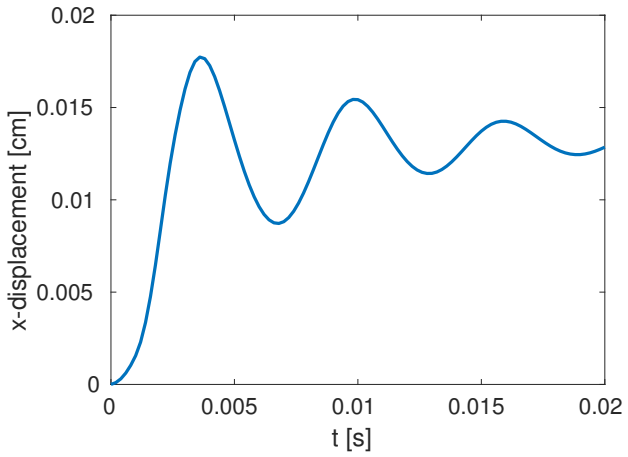

Figure 15: Plot of the x-displacement (in cm) at the center of mass of the structure. Blocking channel test.

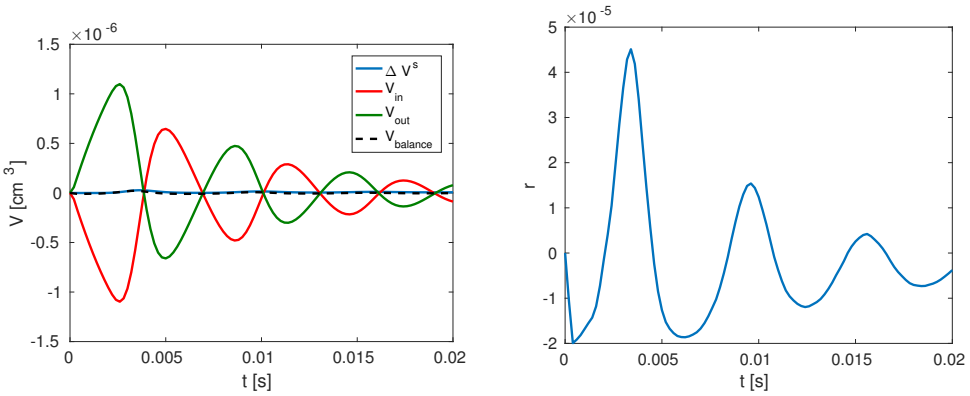

Figure 16: Left: Plot of volumes (in cm^3) ΔV^s, V_{in}, V_{out} and $V_{balance}$ in time. Right: Plot of the relative error of the volume in time. Blocking channel test.

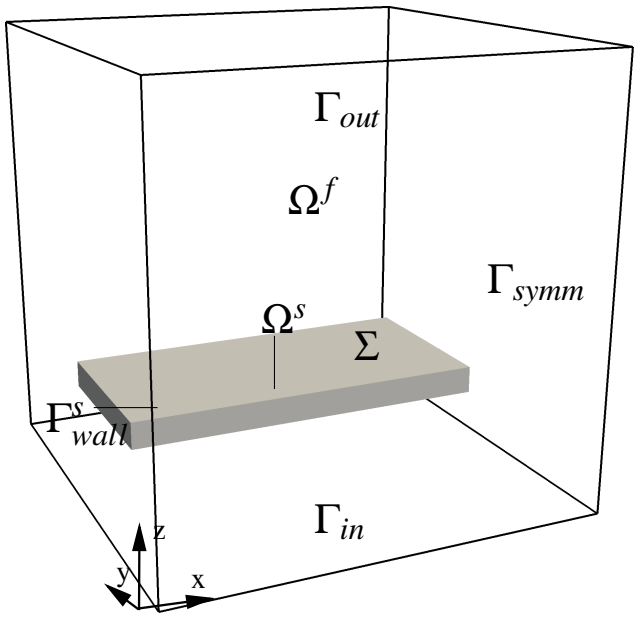

Figure 17: Sketch of the fluid Ω^f and structure Ω^s domains. Non-linear elastic slab test.

fluid elements. The time step Δt is $10^{-3}\,s$. We choose $\gamma_\Sigma = 10^2$ (see equations (11)-(13)), $\gamma_p = 10^3$ (see equation (11)) and $\gamma_g = 1$ (see equation (10)).

In Figure 18, we show the fluid velocity (in cm/s) and the structure displacement (in cm) at four different time steps. The maximum velocity is about $160\,cm/s$ and the maximum displacement reached by the structure is $0.35\,cm$. We see that the method is able to deal with high Reynolds number and large displacement.

In Figure 19, we show the z-displacement (in cm) of the tip of the structure, i.e. at $\mathbf{x}_{tip} = (0.425, 0.25, 0.115)\,cm$, in time.

In Figure 20, we plot the velocity field in the fluid domain and we represent the moving structure accordingly to the computed displacement at different time-steps. We see that the fluid elements crossed by the structure may change in time. We point out that the refinement appearing near the structure is made only for a visualization purpose, in fact the background fluid mesh never changes.

6.3 Ideal aortic valve

In this example, we consider the domain Ω defined by a cylinder of radius $0.5\,cm$ and height $1\,cm$ and three linear immersed structures that are an ideal representation of the leaflets of an aortic valve, see Figure 21. The thickness of the leaflets is $0.02\,cm$. We impose the velocity profile $\mathbf{u} = (0, 0, 50\sin(\frac{\pi}{8}t))\,cm/s$ at the inlet Γ_{in}, we set $\mathbf{T}^f\mathbf{n} = \mathbf{0}$ at the outlet Γ_{out}, and $\mathbf{u} = \mathbf{0}$ on the remaining portions of the fluid boundary. At the fluid-structure interface, we impose the kinematic and dynamic coupling conditions, except on Γ_{wall} where the leaflets are fixed, i.e. $\mathbf{d} = \mathbf{0}$. As initial conditions, we set $\mathbf{u}(\mathbf{x}, 0) = \mathbf{d}(\mathbf{x}, 0) = \dot{\mathbf{d}}(\mathbf{x}, 0) = \mathbf{0}$. We use the following values for the physical parameters:

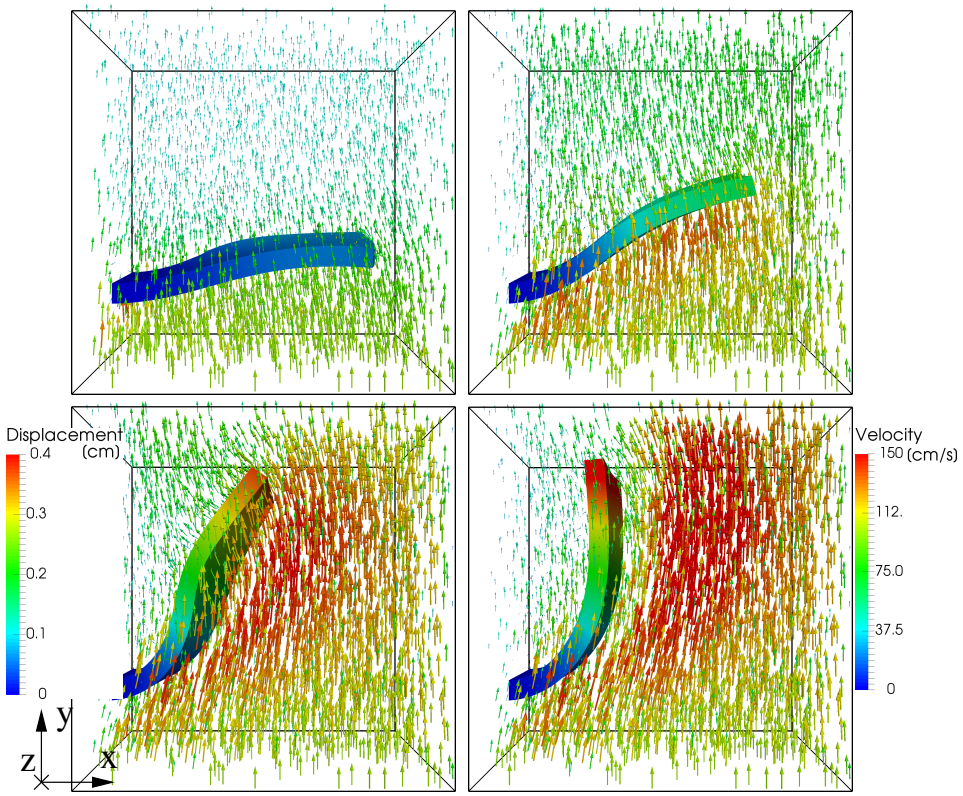

Figure 18: Solution at two different time steps. We plot the fluid velocity (in cm/s) and the solid displacement (in cm). Top, left: $t = 1 \cdot 10^{-3}$. Top, right: $t = 2 \cdot 10^{-3}$. Bottom, left: $t = 4 \cdot 10^{-3}$. Bottom, right: $t = 6 \cdot 10^{-3}$. Non-linear elastic slab test.

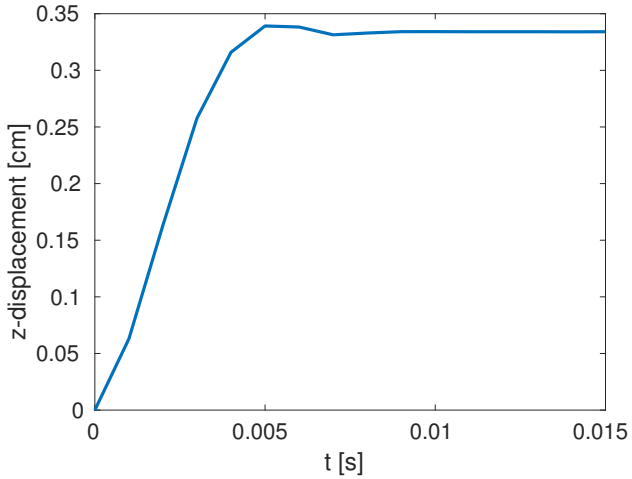

Figure 19: Plot of the z-displacement (in cm) at the tip of the structure in time. Non-linear elastic slab test.

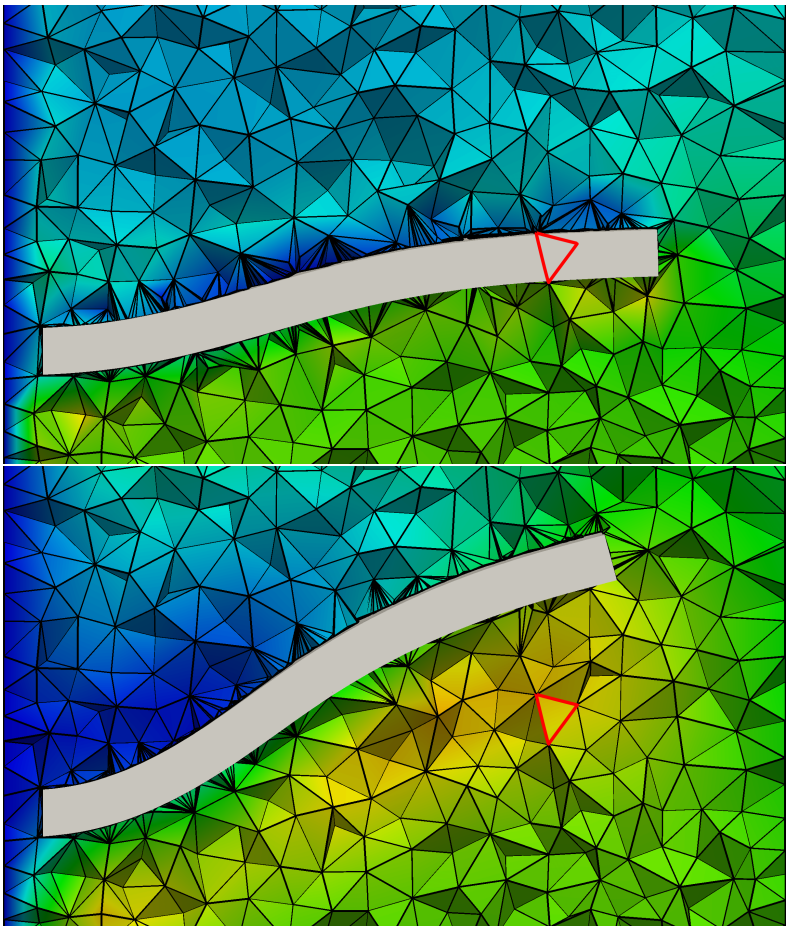

Figure 20: Velocity magnitude on the slice $y = 0.25\,cm$ at time $t = 1 \cdot 10^{-3}s$ (top) and at time $t = 2 \cdot 10^{-3}s$ (bottom). The element highlighted in red at time $t = 1 \cdot 10^{-3}s$ is partially overlapped by the interface, while at time $t = 2 \cdot 10^{-3}s$ is not crossed by the structure. Non-linear elastic slab test.

$\rho^f = 1\,g/cm^3$, $\rho^s = 1.2\,g/cm^3$, $\mu^f = 0.035\,poise$, $\alpha = 1.667 \cdot 10^8\,dyne/cm^2$, $\kappa = 1.724 \cdot 10^7\,dyne/cm^2$ and $\gamma = 1$. We simulate only the initial phase of the movement of the leaflets, i.e. $T = 0.45\,s$. The Reynolds number is equal to $Re = 1430$.

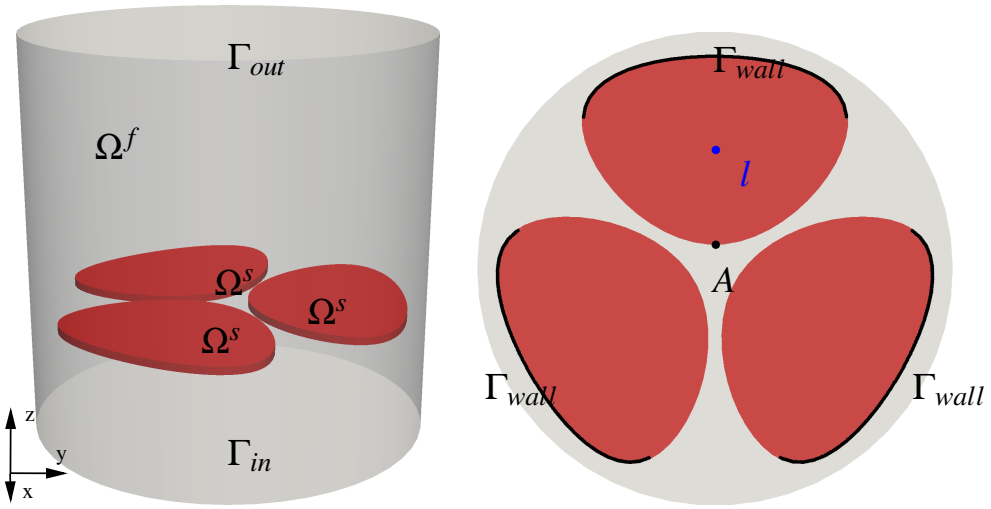

Figure 21: Sketch of the fluid background domain Ω^f and the three foreground domains Ω^s. To the right, we report the top view of the domains. Notice in black the region Γ_{wall} where the leaflets are clamped. Ideal aortic valve test.

For the numerical simulation, we employ a background mesh $\mathcal{T}_h$ of $110 \cdot 10^3$ elements with the average size of the mesh elements $h_{ave} = 0.035\,cm$, while each structure mesh is composed of $16 \cdot 10^3$ elements with $h_{ave} = 0.011\,cm$. We set $\Delta t = 0.05\,s$. We choose $\gamma_\Sigma = 10^2$ (see equations (11)-(13)), $\gamma_p = 10^3$ (see equation (11)) and $\gamma_g = 1$ (see equation (10)).

In what follows we report preliminary results for this test. At the instant where the fluid flow reverses, numerical instabilities occurs. For this reason, we have reported the numerical results until the solution features a stable beaviour. The study of such oscillations is under investigation. A qualitative representation of the solution at time $t = 0.4\,s$ is shown in Figure 22. More specifically, in Figure 23 (left), we plot the z-displacement at the tip (point A in Figure 21) of the three leaflets in time. We observe that the three leaflets behave very similarly during time. In Figure 23 (right), we plot the fluid pressure along line $l : x = 0\,cm$, $y = 0.25\,cm$, $0 \le z \le 1\,cm$ at two different time steps, namely, $t = 0.20s$ and $t = 0.45s$. From this result, we see the different value of the fluid pressure upstream and downstream the leaflet. Notice that, the position of the leaflet (dashed lines) has changed in time.

The maximum z-displacement reached by the leaflets is $0.24\,cm$ and the maximum value of fluid velocity is $17.5\,cm/s$.

In Figure 24, we show the pressure field (in $dyne/cm^2$) and the structure displacement (in cm) on the slice $y = 0.5\,cm$ at time $t = 0.20\,s$ and $t = 0.45\,s$. In particular, we observe the different position of the leaflets with respect to their initial position outlined

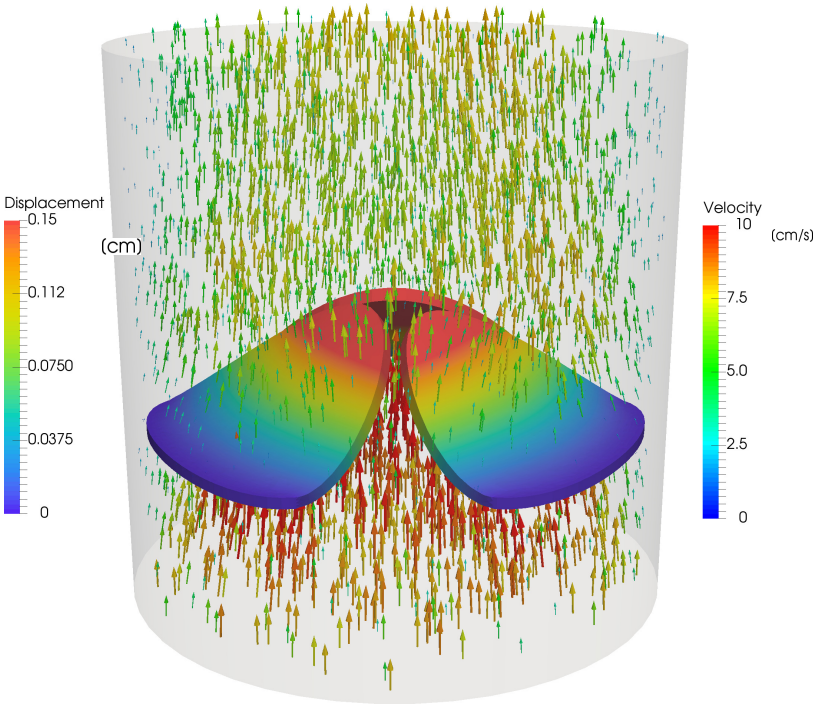

Figure 22: Solution at time $t = 0.4s$. We plot the fluid velocity (in cm/s) and the structure displacement (in cm). Ideal aortic valve test.

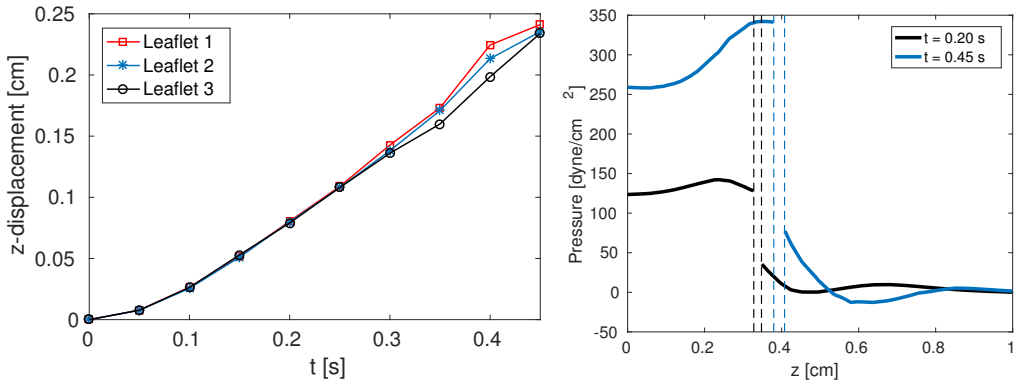

Figure 23: Left: evolution of the displacement (in cm) at the tip of the three leaflets. Right: fluid pressure (in $dyne/cm^2$) along the line l at two different time steps. The position of the leaflet is denoted by the dashed lines. Ideal aortic valve test.

in black. Again, it is possible to see the different values of the fluid pressure upstream and downstream the leaflets.

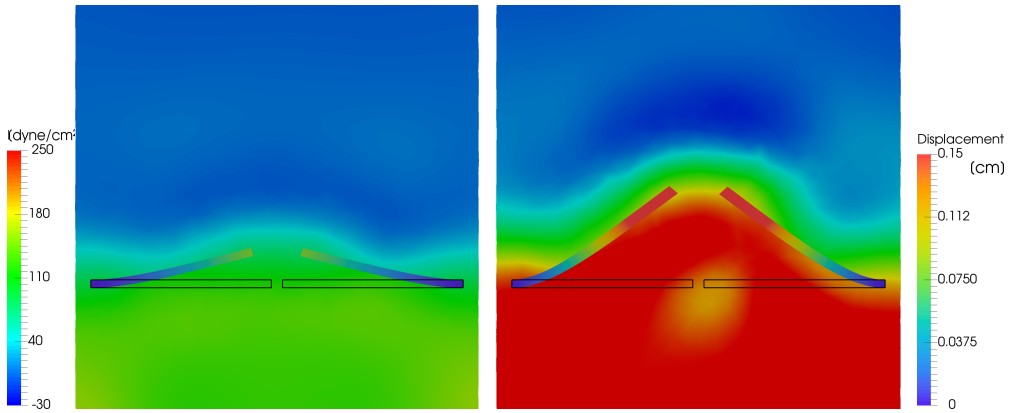

Figure 24: Fluid pressure (in $dyne/cm^2$) and structure displacement (in cm) at slice $y = 0.5cm$. The initial position of the leaflets is denoted by the black lines. Left: time $t = 0.2s$. Right: time $t = 0.45s$. Ideal aortic valve test.

Acknowledgement

The authors gratefully acknowledge the financial support of the Italian MIUR by the grant PRIN12, number 201289A4LX, “Mathematical and numerical models of the cardiovascular system, and their clinical applications”. C. Vergara has been partially supported by the H2020-MSCA-ITN-2017, EU project 765374 ”ROMSOC - Reduced Order Modelling, Simulation and Optimization of Coupled systems”.

References

[1] LifeV. http://www.lifev.org. The parallel finite element library for the solution of PDEs.

[2] F. Alauzet, B. Fabrèges, M. A. Fernández, and M. Landajuela. Nitsche-XFEM for the coupling of an incompressible fluid with immersed thin-walled structures. *Computer Methods in Applied Mechanics and Engineering*, 301:300–335, 2016.

[3] M. Aletti, J.-F. Gerbeau, and D. Lombardi. Modeling autoregulation in three-dimensional simulations of retinal hemodynamics. *Journal for Modeling in Ophthalmology*, 1:88–115, 2015.

[4] C. Annavarapu, M. Hautefeuille, and J. E. Dolbow. A robust Nitsche’s formulation for interface problems. *Computer Methods in Applied Mechanics and Engineering*, 225-228:44–54, 2012.

[5] J. Arciero, A. Harris, B. Siesky, A. Amireskandari, V. Gershuny, A. Pickrell, and G. Guidoboni. Theoretical analysis of vascular regulatory mechanisms contributing to retinal blood flow autoregulationmechanisms contributing to retinal autoregulation. *Investigative ophthalmology & visual science*, 54(8):5584–5593, 2013.

[6] D. N. Arnold, F. Brezzi, B. Cockburn, and L. D. Marini. Unified analysis of discontinuous Galerkin methods for elliptic problems. *SIAM Journal on Numerical Analysis*, 39(5):1749–1779, 2001.

[7] M. Astorino, J.-F. Gerbeau, O. Pantz, and K.-F. Traoré. Fluid-structure interaction and multi-body contact: Application to the aortic valves. *Computer Methods in Applied Mechanics and Engineering*, 198:3603–3612, 2009.

[8] S. Basting, A. Quaini, S. Čanić, and R. Glowinski. Extended ALE Method for fluid–structure interaction problems with large structural displacements. *Journal of Computational Physics*, 331:312–336, 2017.

[9] Y. Bazilevs, M.-C. Hsu, J. Kiendl, R. Wüchner, and K.-U. Bletzinger. 3D simulation of wind turbine rotors at full scale. Part II: Fluid–structure interaction modeling with composite blades. *International Journal for Numerical Methods in Fluids*, 65(1-3):236–253, 2011.

[10] R. Becker, E. Burman, and A. Hansbo. A Nitsche extended finite element method for incompressible elasticity with discontinuous modulus of elasticity. *Computer Methods in Applied Mechanics and Engineering*, 198(41-44):3352–3360, 2009.

[11] A. Beckert and H. Wendland. Multivariate interpolation for fluid-structure-interaction problems using radial basis functions. *Aerospace Science and Technology*, 5(2):125–134, 2001.

[12] T. Belytschko, N. Moës, S. Usui, and C. Parimi. Arbitrary discontinuities in finite elements. *International Journal for Numerical Methods in Engineering*, 50(4):993–1013, 2001.

[13] F. Benedettini, G. Rega, and R. Alaggio. Non-linear oscillations of a four-degree-of-freedom model of a suspended cable under multiple internal resonance conditions. *Journal of sound and vibration*, 182(5):775–798, 1995.

[14] F. Bertrand, P. A. Tanguy, and F. Thibault. A three-dimensional fictitious domain method for incompressible fluid flow problems. *International Journal for Numerical Methods in Fluids*, 25(6):719–736, 1997.

[15] D. Boffi and L Gastaldi. A finite element approach for the immersed boundary method. *Computers & Structures*, 81(8-11):491–501, 2003. K.J Bathe 60th Anniversary Issue.

[16] D. Boffi, L. Gastaldi, and L. Heltai. Numerical stability of the finite element immersed boundary method. *Mathematical Models and Methods in Applied Sciences*, 17(10):1479–1505, 2007.

[17] D. Boffi, L. Gastaldi, L. Heltai, and C. Peskin. On the hyper-elastic formulation of the immersed boundary method. *Computer Methods in Applied Mechanics and Engineering*, 197(25–28):2210–2231, 2008.

[18] I. Borazjani, L. Ge, and F. Sotiropoulos. Curvilinear immersed boundary method for simulating fluid structure interaction with complex 3D rigid bodies. *Journal of Computational physics*, 227(16):7587–7620, 2008.

[19] I. Borazjani, L. Ge, and F. Sotiropoulos. High-resolution fluid–structure interaction simulations of flow through a bi-leaflet mechanical heart valve in an anatomic aorta. *Annals of biomedical engineering*, 38(2):326–344, 2010.

[20] A. L. Braun and A. M. Awruch. Finite element simulation of the wind action over bridge sectional models: Application to the Guamá river bridge (Pará State, Brazil). *Finite Elements in Analysis and Design*, 44(3):105–122, 2008.

[21] E. Burman. Ghost penalty. *C. R. Math. Acad. Sci. Paris*, 348(21-22):1217–1220, 2010.

[22] E. Burman, S. Claus, P. Hansbo, M. G. Larson, and A. Massing. CutFEM: Discretizing geometry and partial differential equations. *International Journal for Numerical Methods in Engineering*, 104(7):472–501, 2015.

[23] E. Burman and M. A. Fernández. An unfitted Nitsche method for incompressible fluid-structure interaction using overlapping meshes. *Computer Methods in Applied Mechanics and Engineering*, 279:497–514, 2014.

[24] E. Burman, M. A. Fernández, and P. Hansbo. Continuous interior penalty finite element method for Oseen's equations. *SIAM Journal on Numerical Analysis*, 44(3):1248–1274, 2006.

[25] E. Burman and M.A. Fernández. Stabilized explicit coupling for fluid-structure interaction using Nitsche's method. *C. R. Acad. Sci. Paris Sér. I Math.*, 345:467–472, 2007.

[26] J. De Hart, F. P. T. Baaijens, G. W. M. Peters, and P. J. G. Schreurs. A computational fluid-structure interaction analysis of a fiber-reinforced stentless aortic valve. *Journal of Biomechanics*, 36(5):699–712, 2003. Cardiovascular Biomechanics.

[27] J. De Hart, G. W. M. Peters, P. J. G. Schreurs, and F. P. T. Baaijens. A three-dimensional computational analysis of fluid–structure interaction in the aortic valve. *Journal of Biomechanics*, 36(1):103–112, 2003.

[28] D. A. Di Pietro and A. Ern. *Mathematical aspects of discontinuous Galerkin methods*, volume 69 of *Mathématiques et Applications*. Springer Berlin Heidelberg, 2012.

[29] J. Donea. An arbitrary Lagrangian-Eulerian finite element method for transient dynamic fluid-structure interaction. *Computer Methods in Applied Mechanics and Engineering*, 33:689–723, 1982.

[30] J. Donea and A. Huerta. *Finite element methods for flow problems*. John Wiley & Sons, 2003.

[31] J. Douglas and T. Dupont. *Interior Penalty Procedures for Elliptic and Parabolic Galerkin Methods*, pages 207–216. Springer Berlin Heidelberg, 1976.

[32] E. H. Dowell and K. C. Hall. Modeling of fluid-structure interaction. *Annual Review of Fluid Mechanics*, 33(1):445–490, 2001.

[33] C. Farhat, M. Lesoinne, and P. Le Tallec. Load and motion transfer algorithms for fluid/structure interaction problems with non-matching discrete interfaces: Momentum and energy conservation, optimal discretization and application to aeroelasticity. *Computer Methods in Applied Mechanics and Engineering*, 157(1-2):95–114, 1998.

[34] L. Formaggia, E. Miglio, A. Mola, and A. Montano. A model for the dynamics of rowing boats. *International journal for numerical methods in fluids*, 61(2):119–143, 2009.

[35] L. Formaggia, E. Miglio, A. Mola, and N. Parolini. Fluid–structure interaction problems in free surface flows: application to boat dynamics. *International journal for numerical methods in fluids*, 56(8):965–978, 2008.

[36] L. Ge and F. Sotiropoulos. A numerical method for solving the 3D unsteady incompressible Navier–Stokes equations in curvilinear domains with complex immersed boundaries. *Journal of Computational Physics*, 225(2):1782–1809, 2007.

[37] A. Gerstenberger. *An XFEM based fixed-grid approach to fluid-structure interaction*. PhD thesis, Technical University of Munich, 2010.

[38] A. Gerstenberger and W. A. Wall. An extended finite element method based approach for large deformation fluid-structure interaction. In P. Wesseling, E. Onate, and J. Periaux, editors, *Proceedings of the European Conference on Computational Fluid Dynamics*, 2006.

[39] A. Gerstenberger and W. A. Wall. An extended finite element method/Lagrange multiplier based approach for fluid–structure interaction. *Computer Methods in Applied Mechanics and Engineering*, 197(19):1699–1714, 2008.

[40] A. Gerstenberger and W. A. Wall. An embedded Dirichlet formulation for 3D continua. *International Journal for Numerical Methods in Engineering*, 82(5):537–563, 2010.

[41] R. Glowinski, T.-W. Pan, T. I. Hesla, and D. D. Joseph. A distributed lagrange multiplier/fictitious domain method for particulate flows. *International Journal of Multiphase Flow*, 25(5):755–794, 1999.

[42] R. Glowinski, T.-W. Pan, T. I. Hesla, D. D. Joseph, and J. Periaux. A fictitious domain approach to the direct numerical simulation of incompressible viscous flow past moving rigid bodies: application to particulate flow. *Journal of Computational Physics*, 169(2):363–426, 2001.

[43] R. Glowinski, T.-W. Pan, and J. Periaux. A fictitious domain method for Dirichlet problem and applications. *Computer Methods in Applied Mechanics and Engineering*, 111(3-4):283–303, 1994.

[44] R. Glowinski, T.-W. Pan, and J. Periaux. A fictitious domain method for external incompressible viscous flow modeled by Navier-Stokes equations. *Computer Methods in Applied Mechanics and Engineering*, 112(1):133–148, 1994.

[45] R. Glowinski, T.-W. Pan, and J. Periaux. A Lagrange multiplier/fictitious domain method for the numerical simulation of incompressible viscous flow around moving rigid bodies:(I) case where the rigid body motions are known a priori. *Comptes Rendus de l'Académie des Sciences-Series I-Mathematics*, 324(3):361–369, 1997.

[46] B. E. Griffith. Immersed boundary model of aortic heart valve dynamics with physiological driving and loading conditions. *International Journal for Numerical Methods in Biomedical Engineering*, 28(3):317–345, 2012.

[47] B. E. Griffith, R. D. Hornung, D. M. McQueen, and C. S. Peskin. An adaptive, formally second order accurate version of the immersed boundary method. *Journal of Computational Physics*, 223(1):10–49, 2007.

[48] B.E. Griffith, X. Luo, D.M. McQueen, and C.S. Peskin. Simulating the fluid dynamics of natural and prosthetic heart valves using the immersed boundary method. *International Journal of Applied Mechanics*, 1:137–176, 2009.

[49] A. Hansbo and P. Hansbo. An unfitted finite element method, based on Nitsche's method, for elliptic interface problems. *Computer Methods in Applied Mechanics and Engineering*, 191(47–48):5537–5552, 2002.

[50] A. Hansbo and P. Hansbo. A finite element method for the simulation of strong and weak discontinuities in solid mechanics. *Computer Methods in Applied Mechanics and Engineering*, 193(33-35):3523–3540, 2004.

[51] A. Hansbo, P. Hansbo, and M. G. Larson. A finite element method on composite grids based on Nitsche's method. *ESAIM: Mathematical Modelling and Numerical Analysis*, 37(3):495–514, 2003.

[52] P. Hansbo, M. G. Larson, and S. Zahedi. A cut finite element method for a Stokes interface problem. *Applied Numerical Mathematics*, 85:90–114, 2014.

[53] P. Hansbo, M. G. Larson, and S. Zahedi. Characteristic cut finite element methods for convection–diffusion problems on time dependent surfaces. *Computer Methods in Applied Mechanics and Engineering*, 293:431–461, 2015.

[54] Z. Harun, E. Reda, and S. Abdullah. Large eddy simulation of the wind flow over skyscrapers. *Recent Advances in Mechanics and Mechanical Engineering*, 15:72–79, 2015.

[55] C. W. Hirt, A. A. Amsden, and J. L. Cook. An arbitrary lagrangian-eulerian computing method for all flow speeds. *Journal of computational physics*, 14(3):227–253, 1974.

[56] M.-C. Hsu, D. Kamensky, Y. Bazilevs, M. S. Sacks, and T.J.R. Hughes. Fluid–structure interaction analysis of bioprosthetic heart valves: significance of arterial wall deformation. *Computational Mechanics*, 54(4):1055–1071, 2014.

[57] T. J. R. Hughes and G. M. Hulbert. Space-time finite element methods for elastodynamics: formulations and error estimates. *Computer Methods in Applied Mechanics and Engineering*, 66(3):339–363, 1988.

[58] T. J. R. Hughes, W. K. Liu, and T. K. Zimmermann. Lagrangian-Eulerian finite element formulation for incompressible viscous flows. *Computer Methods in Applied Mechanics and Engineering*, 29(3):329–349, 1981.

[59] C. Johnson, U. Nävert, and J. Pitkäranta. Finite element methods for linear hyperbolic problems. *Computer Methods in Applied Mechanics and Engineering*, 45(1-3):285–312, 1984.

[60] T. Jonsson, M. G. Larson, and K. Larsson. Cut finite element methods for elliptic problems on multipatch parametric surfaces. *Computer Methods in Applied Mechanics and Engineering*, 324:366–394, 2017.

[61] R. Kamakoti and W. Shyy. Fluid–structure interaction for aeroelastic applications. *Progress in Aerospace Sciences*, 40(8):535–558, 2004.

[62] D. Kamensky, M.-C. Hsu, D. Schillinger, J.A. Evans, A. Aggarwal, A. Bazilevs, M.S. Sacks, and T.J.R. Hughes. An immersogeometric variational framework for fluidstructure interaction: Application to bioprosthetic heart valves. *Computer Methods in Applied Mechanics and Engineering*, 284:1005–1053, 2015.

[63] S. Katayama, N. Umetani, S. Sugiura, and T. Hisada. The sinus of Valsalva relieves abnormal stress on aortic valve leaflets by facilitating smooth closure. *The Journal of thoracic and cardiovascular surgery*, 136(6):1528–1535, 2008.

[64] Y. G. Lai, K. B. Chandran, and J. Lemmon. A numerical simulation of mechanical heart valve closure fluid dynamics. *Journal of Biomechanics*, 35(7):881–892, 2002.

[65] T. B. Le and F. Sotiropoulos. Fluid–structure interaction of an aortic heart valve prosthesis driven by an animated anatomic left ventricle. *Journal of Computational Physics*, 244:41–62, 2013.

[66] W. K. Liu, Y. Liu, D. Farrell, L. T. Zhang, X. S. Wang, Y. Fukui, N. Patankar, Y. Zhang, C. Bajaj, J. Lee, J. Hong, X. Chen, and H. Hsu. Immersed finite element method and its applications to biological systems. *Computer Methods in Applied Mechanics and Engineering*, 195(13):1722–1749, 2006.

[67] G. Marom. Numerical methods for fluid–structure interaction models of aortic valves. *Archives of Computational Methods in Engineering*, 22(4):595–620, 2015.

[68] A. Massing, M. G. Larson, and A. Logg. Efficient implementation of finite element methods on nonmatching and overlapping meshes in three dimensions. *SIAM Journal on Scientific Computing*, 35(1):C23–C47, 2013.

[69] A. Massing, M. G. Larson, A. Logg, and M. E. Rognes. A stabilized Nitsche overlapping mesh method for the Stokes problem. *Numerische Mathematik*, 128(1):73–101, 2014.

[70] A. Massing, M. G. Larson, A. Logg, and M. E. Rognes. A Nitsche-based cut finite element method for a fluid-structure interaction problem. *Communications in Applied Mathematics and Computational Science*, 10(2):97–120, 2015.

[71] U. M. Mayer, A. Popp, A. Gerstenberger, and W. A. Wall. 3D fluid-structure-contact interaction based on a combined XFEM FSI and dual mortar contact approach. *Computational Mechanics*, 46(1):53–67, 2010.

[72] R. Mittal and G. Iaccarino. Immersed boundary methods. *Annual Review of Fluid Mechanics*, 37(1):239–261, 2005.

[73] N. Moës, J. Dolbow, and T. Belytschko. A finite element method for crack growth without remeshing. *International Journal for Numerical Methods in Engineering*, 46:131–150, 1999.

[74] G. Morgenthal. *Fluid Structure Interaction in Bluff-body Aerodynamics and Long-span Bridge Design: Phenomena and Methods*. University of Cambridge, Department of Engineering Cambridge, 2000.

[75] Y. S. Morsi, W. W. Yang, C. S. Wong, and S. Das. Transient fluid–structure coupling for simulation of a trileaflet heart valve using weak coupling. *Journal of artificial organs*, 10(2):96–103, 2007.

[76] H. Nguyen and J. Reynen. A space-time least-square finite element scheme for advection-diffusion equations. *Computer Methods in Applied Mechanics and Engineering*, 42(3):331–342, 1984.

[77] S. Nicaise, Y. Renard, and E. Chahine. Optimal convergence analysis for the extended finite element method. *International Journal for Numerical Methods in Engineering*, 86(4-5):528548, 2011.

[78] N. Parolini and A. Quarteroni. Mathematical models and numerical simulations for the America's cup. *Computer Methods in Applied Mechanics and Engineering*, 194(9):1001–1026, 2005.

[79] C. Peskin. Flow patterns around heart valves: A numerical method. *Journal of Computational Physics*, 10(2):252–271, 1972.

[80] M. J. Pettigrew and C. E. Taylor. Vibration analysis of shell-and-tube heat exchangers: an overview - Part 1: flow, damping, fluidelastic instability. *Journal of fluids and structures*, 18(5):469–483, 2003.

[81] G. Rega. Nonlinear vibrations of suspended cables–Part I: Modeling and analysis. *Applied Mechanics Reviews*, 57(6):443–478, 2004.

[82] B. Schott and W. A. Wall. A new face-oriented stabilized XFEM approach for 2D and 3D incompressible Navier-Stokes equations. *Computer Methods in Applied Mechanics and Engineering*, 276:233–265, 2014.

[83] J. M. A. Stijnen, J. De Hart, P. H. M. Bovendeerd, and F. N. van de Vosse. Evaluation of a fictitious domain method for predicting dynamic response of mechanical heart valves. *Journal of Fluids and Structures*, 19(6):835–850, 2004.

[84] R. Temam. *Navier-Stokes Equations*. 1977.

[85] C. Trivedi and M. J. Cervantes. Fluid-structure interactions in francis turbines: A perspective review. *Renewable and Sustainable Energy Reviews*, 68:87–101, 2017.

[86] R. van Loon. *A 3D method for modelling the fluid-structure interaction of heart valves*. PhD thesis, Technische Universiteit Eindhoven, 2005.

[87] R. van Loon, P. D. Anderson, and F. N. van de Vosse. A fluid–structure interaction method with solid-rigid contact for heart valve dynamics. *Journal of Computational Physics*, 217(2):806–823, 2006.

[88] R. van Loon, P. D. Anderson, F. N. van de Vosse, and S. J. Sherwin. Comparison of various fluid–structure interaction methods for deformable bodies. *Computers & Structures*, 85(11-14):833–843, 2007. Fourth MIT Conference on Computational Fluid and Solid Mechanics.

[89] E. Votta, T. B. Le, M. Stevanella, F. Fusini, E. G. Caiani, A. Redaelli, and F. Sotiropoulos. Toward patient-specific simulations of cardiac valves: State-of-the-art and future directions. *Journal of Biomechanics*, 46(2):217–228, 2013. Special Issue: Biofluid Mechanics.

[90] X. Wang and W. K. Liu. Extended immersed boundary method using FEM and RKPM. *Computer Methods in Applied Mechanics and Engineering*, 193(12):1305–1321, 2004.

[91] E. J. Weinberg, P. J. Mack, F. J. Schoen, G. García-Cardeña, and M. R. K. Mofrad. Hemodynamic environments from opposing sides of human aortic valve leaflets evoke distinct endothelial phenotypes in vitro. *Cardiovascular engineering*, 10(1):5–11, 2010.

[92] H. Zhang, L. Liu, M. Dong, and H. Sun. Analysis of wind-induced vibration of fluid–structure interaction system for isolated aqueduct bridge. *Engineering structures*, 46:28–37, 2013.

[93] L. T. Zhang and M. Gay. Immersed finite element method for fluid-structure interactions. *Journal of Fluids and Structures*, 23(6):839–857, 2007.

[94] L. T. Zhang, A. Gerstenberger, X. Wang, and W. K. Liu. Immersed finite element method. *Computer Methods in Applied Mechanics and Engineering*, 193(21):2051–2067, 2004.

[95] S. Zonca, C. Vergara, and L. Formaggia. An unfitted formulation for the interaction of an incompressible fluid with a thick structure via an XFEM/DG approach. *SIAM Journal on Scientific Computing*, 40(1):B59–B84, 2018.

MOX Technical Reports, last issues

Dipartimento di Matematica
Politecnico di Milano, Via Bonardi 9 - 20133 Milano (Italy)

25/2018 Chave, F.; Di Pietro, D.A.; Formaggia, L.
A Hybrid High-Order method for passive transport in fractured porous media

24/2018 Bassi, C.; Abbà, A.; Bonaventura,L.; Valdettaro,L.
Direct and Large Eddy Simulation of three-dimensional non-Boussinesq gravity currents with a high order DG method

21/2018 Gervasio, P.; Dede', L.; Chanon, O.; Quarteroni, A.
Comparing Isogeometric Analysis and Spectral Element Methods: accuracy and spectral properties

22/2018 Pegolotti, L.; Dede', L.; Quarteroni, A.
Isogeometric Analysis of the electrophysiology in the human heart: numerical simulation of the bidomain equations on the atria

23/2018 Benacchio, T.;Bonaventura,L.
A seamless extension of DG methods for hyperbolic problems to unbounded domains

20/2018 Bassi, C. ; Abbà, A.; Bonaventura L.; Valdettaro, L.
A priori tests of a novel LES approach to compressible variable density turbulence

19/2018 Menghini, F.; Dede', L.; Quarteroni, A.
Variational Multiscale LES modeling of blood flow in an idealized left human heart

18/2018 Antonietti, P.F.; Bonaldi, F.; Mazzieri, I.
A high-order discontinuous Galerkin approach to the elasto-acoustic problem

17/2018 Agosti, A.; Giverso, C.; Faggiano, E.;Stamm,A.; Ciarletta, P.
A personalized mathematical tool for neuro-oncology: a clinical case study

15/2018 Simona, A.; Bonaventura, L.; Pugnat, T.; Dalena, B.
High order time integrators for the simulation of charged particle motion in magnetic quadrupoles